

Title: [Lifetime estimation of IGBT power modules]
Semester: [10th semester]
Semester theme: [Master Thesis]
Project period: [11.03.2013 – 09.08.2013]
ECTS: [30]
Supervisor: [Stig Munk-Nielsen]
Project group: [PED4-1049]

[Laura Nicola]

Copies: [2] stk.
Pages total: [63] sider
Appendix: [3]
Supplements: [1 CD]

SYNOPSIS: *Power modules are one of the least reliable components in electrical systems functioning in harsh environments. Lifetime estimation of the modules has become a critical issue. The study case under focus is of a power supply for a particle accelerator system. The mission profile has an application specific pattern and it is irregular. An electro-thermal model using PLECS toolbox has been implemented to determine the junction temperature of the chips. Rainflow analysis has been employed to identify the mean and temperature swings of each cycle. An analytical lifetime estimation model based on the Coffin-Manson law considering both the average and temperature ranges is used. With Palmgren Miner rule the damage produced on the transistor is quantified. Lifetime predictions are made for three scenarios on a part of the mission profile.*

By signing this document, each member of the group confirms that all group members have participated in the project work, and thereby all members are collectively liable for the contents of the report. Furthermore, all group members confirm that the report does not include plagiarism.

Acknowledgments

I would like to express my gratitude to my supervisor Stig Munk-Nielsen for his continuous guidance and support throughout the project. To Rasmus Ørndrup Nielsen, PhD student at Danfysik A/S, Michael Budde and Søren Viner Weber from Danfysik for providing the data and replying to my questions in a very prompt manner.

To all my friends for their moral support and advices, especially to Ovidiu Nicolae Faur and Bogdan Incau.

Last but not least, to my family.

Laura Nicola

9th of August 2013, Aalborg

Table of contents

Acknowledgments	3
Table of contents	5
List of figures	7
List of tables	9
1. Introduction	11
1.1. Background.....	11
1.2. Study case.....	11
1.3. Motivation	13
1.4. Methodology.....	14
1.5. Limitations.....	15
2. System modeling	16
2.1. Converter principle of operation.....	16
2.2. Converter modeling	16
2.3. Electrical circuit and controller design.....	17
2.4. Power loss model.....	20
2.5. Thermal modelling of IGBT power modules	22
2.6. Simulation results	24
2.7. Summary.....	25
3. Lifetime modelling	26
3.1 Rainflow cycle counting method.....	26
3.2. Coffin Manson law	29
3.3. Damage modelling.....	30
3.4. Lifetime estimation.....	30
3.5. Simulation results	30
3.6. Simulation with increased water temperature.....	38
3.7. Summary.....	40
4. Conclusion.....	42
4.1. Contributions	42
4.2. Limitations.....	42
5. Future work	43

Bibliography	45
Appendix A	47
Appendix B.....	56
Appendix C.....	59

List of figures

Figure 1 Single phase H bridge converter topology	11
Figure 2 The DF1400R12IP4D IGBT power module [1].....	12
Figure 3 Pattern of the current across the load (not to scale) [source: Danfysik].....	12
Figure 4 Internal structure of a typical multilayer IGBT power converter module (left) [2] and	13
Figure 5 For the Doubly Fed Induction Generator topology: Grid-side converter: junction temperature on the IGBT and diode chips at 50Hz (left) and Generator-side converter: temperature junction on diode and IGBT chips at 1 Hz (right) [4].....	14
Figure 6 Flowchart of remaining fatigue lifetime determination of the of IGBT power modules	14
Figure 7 Operation of an H bridge converter in quadrat I and IV	16
Figure 8 Flow chart of obtaining the junction temperature in PLECS	16
Figure 9 Closed loop control of the H bridge converter	17
Figure 10 Block diagram of the H bridge converter	17
Figure 11 Open loop Bode diagram of the system.....	19
Figure 12 Time response to a step input of the system.....	20
Figure 13 Conduction power losses: a.) of IGBT; b.) of the diode.....	21
Figure 14 Switching power losses of IGBT: a.) On state; b.) Off state	22
Figure 15 Off state energy loss of the diode	22
Figure 16 Thermal impedance variation with time: a.) for IGBT; b.) for diode [1].....	23
Figure 17 Foster representation of IGBT/diode.....	23
Figure 18 Block diagram of thermal model implementation in PLECS.....	24
Figure 19 Current waveform on active components	24
Figure 20 Total power loss and junction temperature on first leg elements	25
Figure 21 Total power loss and junction temperature on second leg elements	25
Figure 22 Flowchart of remaining fatigue lifetime estimation	26
Figure 23 Identification of the extrema from a regular junction temperature profile in Matlab	26
Figure 24 Three point counting method: extracting half cycles at the starting points and counting a half cycle from P1 to P2 [9].....	27
Figure 25 Rainflow cycle counting technique applied on the sequence of extrema.....	27
Figure 26 Rainflow cycle counting technique performed in Matlab on the sequence of extrema	28
Figure 27 Parameters of an irregular temperature loading	28
Figure 28 Expected number of cycles to failure as a dependence of the change in temperature obtained through curve fitting [11]	29
Figure 29 Irregular current loading history	31
Figure 30 Junction temperature profile on IGBT1, Diode1, IGBT2 and Diode2.....	31
Figure 31 Rainflow 3D matrix showing the distribution of temperature ranges and average temperature among the counted cycles for IGBT1 and Diode1.....	32
Figure 32 Rainflow 3D matrix showing the distribution of temperature ranges and average temperature among the counted cycles for Diode2.....	32
Figure 33 Resemblance of power modules inside the converter	32
Figure 34 Damage histogram of IGBT1	33

Figure 35 Rainflow histogram of the difference in temperature among counted cycles and the produced damage for Diode1	33
Figure 36 Rainflow histogram of the distribution of difference temperature among the counted cycles and the damage produced on Diode2	34
Figure 37 Current profile with the 'chimney' removed	35
Figure 38 Junction temperature variation on IGBT1, Diode1, IGBT2 and Diode2	35
Figure 39 Rainflow 3D matrix for IGBT and Diode1	36
Figure 40 Rainflow 3D matrix for Diode2.....	36
Figure 41 Rainflow and damage histograms on IGBT1	36
Figure 42 Rainflow and damage histograms on Diode1	37
Figure 43 Rainflow and damage histograms of Diode2	37
Figure 44 Rainflow 3D matrices for IGBT and Diode 1	38
Figure 45 Rainflow 3D matrix for Diode 2.....	38
Figure 46 Part of temperature profile when the water temperature gets increased to 80°C	39
Figure 47 Rainflow histograms of the distribution of ranges of temperature among cycles and the produced damage for IGBT	39
Figure 48 Rainflow histograms of the distribution of ranges of temperature among cycles and the produced damage for Diode1	40
Figure 49 Rainflow histograms of the distribution of ranges of temperature among cycles and the produced damage for Diode2.....	40
Figure 50 Example of how the extrema are identified on a loading history part.....	59
Figure 51 Identified extrema from the loading history	59
Figure 52 Example of how the three-point check algorithm is working. Removal of P ₁	60
Figure 53 Example of how the three-point check algorithm is working. Removal of P ₄ and P ₅	60
Figure 54 Example of how the three-point check algorithm is working. Removal of P ₂	60
Figure 55 Example of how the three-point check algorithm is working. Removal of P ₆ and P ₇	61
Figure 56 Example of how the three-point check algorithm is working. Removal of P ₈ and P ₉	61
Figure 57 Example of how the three-point check algorithm is working. Removal of P ₁₀ and P ₁₁	61
Figure 58 Example of how the three-point check algorithm is working. Removal of P ₁₂ and P ₁₃ .	61
Figure 59 Example of how the three-point check algorithm is working. Removal of P ₁₄ and P ₁₅ .	62
Figure 60 Example of how the Rainflow three point check algorithm is done using Matlab	62
Figure 61 Rainflow 3D matrix containing the range (shown here as twice the amplitude), mean stress and number of cycles	63
Figure 62 Rainflow histogram of the distribution of range temperature among the identified cycles (left) and the damage cause by the ranges (right)	63

List of tables

<i>Table 1 List of main parameters of the converter [source Danfysik]</i>	12
<i>Table 2 Main parameters of DF1400R12IP4D IGBT power module</i>	12
<i>Table 3 Wear-out failure mechanisms and causes of power converters [4]</i>	13
<i>Table 4 Summary of simulations results</i>	41
<i>Table 5 IGBT turn-on energy data points for 25°C</i>	56
<i>Table 6 IGBT turn-on energy data points for 125°C</i>	56
<i>Table 7 IGBT turn-on energy data points for 150°C</i>	56
<i>Table 8 IGBT turn-off energy data points for 25°C</i>	56
<i>Table 9 IGBT turn-off energy data points for 125°C</i>	56
<i>Table 10 IGBT turn-off energy data points for 150°C</i>	57
<i>Table 11 IGBT conduction losses</i>	57
<i>Table 12 Diode conduction losses point data</i>	57
<i>Table 13 Losses during reverse recovery for 125°C</i>	57
<i>Table 14 Losses during reverse recovery for 150°C</i>	57
<i>Table 15 Foster parameters of the IGBT chip</i>	58
<i>Table 16 Foster parameters of the diode chip</i>	58
<i>Table 17 Heatsink and water cooling system Foster parameters (SOURCE: Danfysik)</i>	58
<i>Table 18 Values of the identified extrema points</i>	59
<i>Table 19 Rainflow matrix containing the temperature ranges, mean temperature and number of cycles</i>	62



1. Introduction

1.1. Background

Reliability, cost and time to market are the three main constraints of any product [1]. According to an industry-based survey in 2009 the converter is one of the most unreliable components of electrical systems that are operating in harsh environments [2]. The system reliability can be improved if the converter is replaced before it fails. Thus, the lifetime estimation of power converters is a critical issue.

In order to determine the reliability of a product tests have to be performed on the component under different loading conditions. For the case of IGBT devices testing under normal operating conditions is impractical, costly and is requiring long time to market, as their life is relatively long. To overcome these aspects accelerated life testing (ALT) is used for determining their reliability and estimation of lifetime expectancy. By using this testing methodology the devices under test are subjected to more severe environmental conditions than the normal operating conditions in order to induce failures in a shorter period of time. The results are then analyzed to assess the reliability, lifetime expectancy and degradation of the component under normal operating conditions [1]. Accelerated life testing on IGBTs is performed with thermal and power cycling testing setups [3].

Other lifetime prediction models are the analytical ones. Analytical lifetime models estimate the life of an IGBT power module in terms of number of cycles to failure considering different factors like temperature swing, average temperature, bond wire current and frequency. The problem with these models is to accurately identify, extract and count the cycles from the junction temperature profile. The most commonly used cycle counting method for accurately extracting thermal cycles within the temperature profile is the Rainflow analysis. The analytical lifetime modeling is done with the use of Palmgren Miner rule. It assumes that each identified thermal cycle produces some degree of damage on the IGBT and thus it contributes to the life consumption of the device [3].

Within this project an analytical model will be used for estimating the lifetime of the IGBT power modules.

1.2. Study case

The study case of the project is about a converter designed for an accelerator particle used for chemo treatment. The power supply under focus is considered as a 2 quadrant dc chopper topology that functions in the 1st and 4th quadrant with a series RL that models a magnet, as it can be seen in Figure 1 [4]:

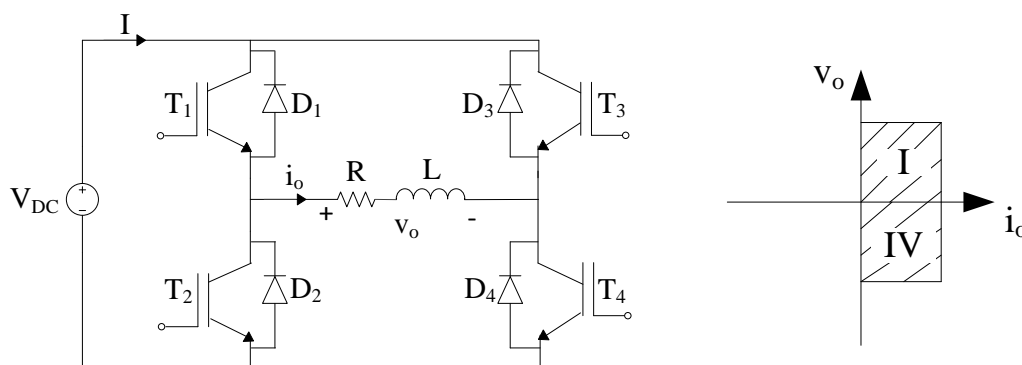


Figure 1 Single phase H-bridge converter topology [4]

The main parameters of the converter are summarized in Table 1:

Table 1 List of main parameters of the converter [source Danfysik]

Parameter	Value	Measure
V_{DC}	400	V
f_{sw}	17800	Hz
R	0.112	Ω
L	0.135	H

The power module used within the H-bridge converter is DF1400R12IP4D from Infineon. Its datasheet is attached in Appendix A. The typical application of the power module is as a chopper and it includes an IGBT transistor and two diodes as it can be seen in Figure 2:

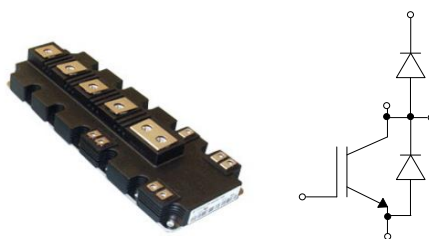


Figure 2 The DF1400R12IP4D IGBT power module [5]

The main parameters of the power module provided in the datasheet [5] are listed in Table 2:

Table 2 Main parameters of DF1400R12IP4D IGBT power module [5]

Parameter	Symbol	Value
Collector-emitter voltage	V_{CE}	1200 V
Collector current	I_{Cnom}	1400 A
Total power dissipation	P_{tot}	7.7 kW
IGBT thermal resistance, junction to case (max)	R_{thJC}	19.5K/kW
IGBT thermal resistance, case to heatsink (typ)	R_{thCH}	9.30K/kW
IGBT turn on switching losses (@ 312.5 A, 25°C)	E_{on}	11 mJ
IGBT turn off switching losses (@ 312.5 A, 25°C)	E_{off}	67 mJ
IGBT conduction losses (@ 312.5 A, 25°C)	P_{cond}	315 W

The power modules are modeled using discrete semiconductor devices. In the real application because of the high current demand (1250 [A]), T_1 and T_4 , which enclose the main current path, are implemented using 4 paralleled power modules. T_2 and T_3 locations contain a single module. The current profile flowing through the load has the standard pattern depicted in Figure 3.

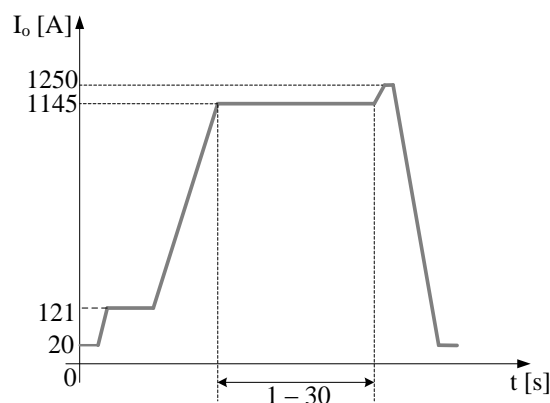


Figure 3 Pattern of the current across the load (not to scale) [source: Danfysik]

The application requires that the current always starts at 20A, goes until 1250A all the time (this increase is called ‘chimney’) and returns to 20A, so that the electromagnetic field stays the same on the magnet. The levels of current in between may vary. Also the length of a cycle is variable and it can last between 1 and 30s. Because there are 4 modules in parallel, in the simulation the current is divided by 4.

1.3. Motivation

Due to high variation of the load current, the IGBTs are subjected to large temperature swings. The inside material layers of power modules have different thermal expansion coefficients and when exposed to temperature swings micro-movements are taking place between the layers. The thermo-mechanical stresses are affecting primarily the soldering and the wire bonding [6]. With time this process called fatigue leads to failure.

Figure 4 depicts the internal structure of a typical multilayer IGBT power module and the coefficients of thermal expansion (CTE) for the most common layer materials. It can be seen that aluminum has a much higher CTE than silicon, followed by copper. The critical fatigue-related areas are considered to be the solder and the boundary between Al bonding wires and Si chips [6].

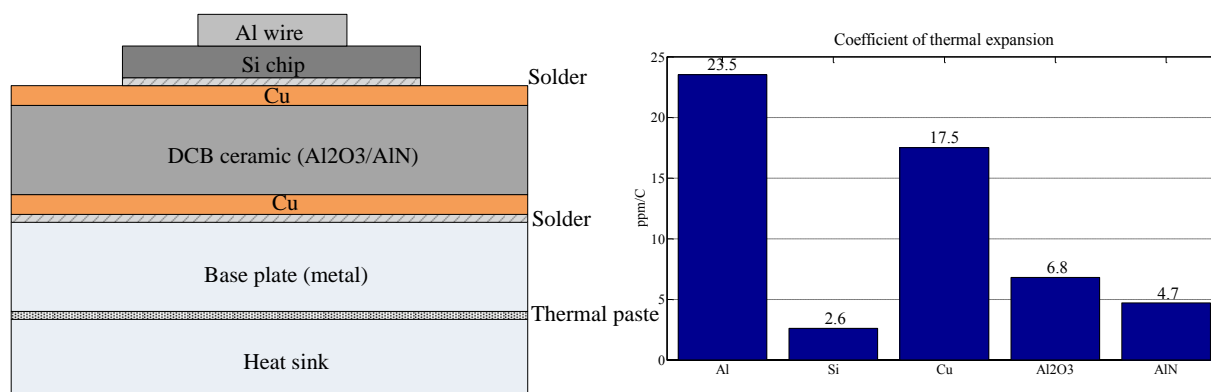


Figure 4 Internal structure of a typical multilayer IGBT power converter module (left) [6] and Coefficients of thermal expansion for material layers inside the IGBT power converter [3]

. The most common fatigue-related failure mechanism and causes are summarized in Table 3:

Table 3 Wear-out failure mechanisms and causes of power converters [7]

	Failure mechanisms	Failure causes
Wear out failures	<ul style="list-style-type: none"> • bond wire lift-off • solder fatigue 	frequent thermal cycling and difference in thermal expansion coefficients (TEC) of material layers
	<ul style="list-style-type: none"> • degradation of thermal grease 	ageing
	<ul style="list-style-type: none"> • fretting corrosion at pressure contacts 	vibration or difference in TEC
	<ul style="list-style-type: none"> • tin whiskers 	compressive mechanical stress

Also, it has been noticed in wind turbines applications that at low frequency the junction temperature on the IGBTs and diodes follow the pattern of the current and so, resulting a temperature variation as it is shown in Figure 5:

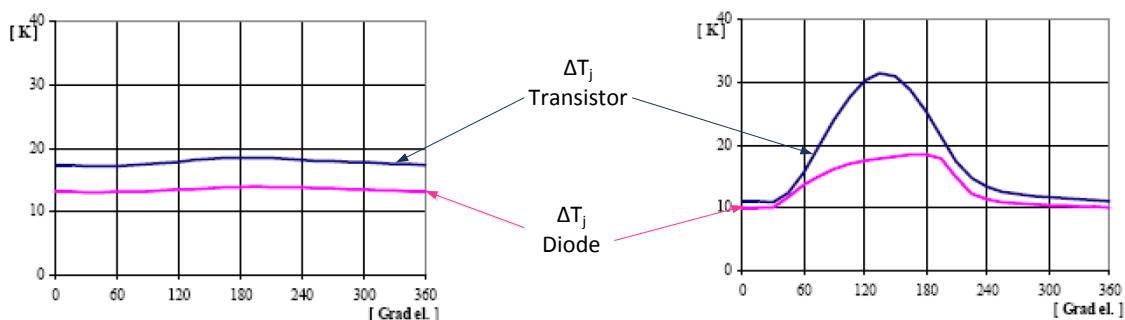


Figure 5 For the Doubly Fed Induction Generator topology: Grid-side converter: junction temperature on the IGBT and diode chips at 50Hz (left) and Generator-side converter: temperature junction on diode and IGBT chips at 1 Hz (right) [7]

The mission profile of the power modules, i.e. loading current was provided by Danfysik and it was noticed that it has a variable low frequency. It is expected that the junction temperature will follow the current pattern similar to the case presented in Figure 5.

1.4. Methodology

Figure 6 shows the steps of the analytical model that has been decided to be used for determining of the remaining fatigue life of the power modules:

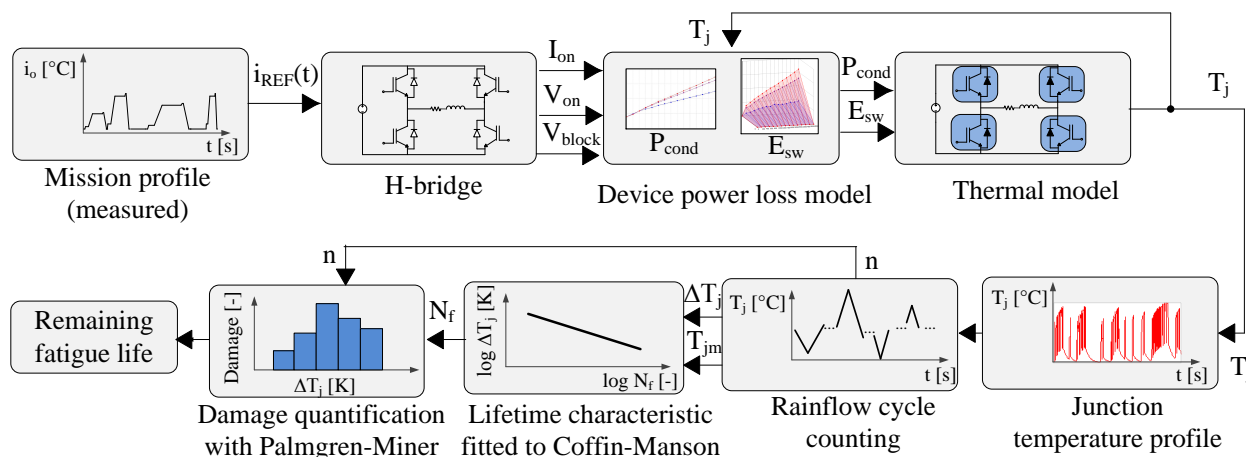


Figure 6 Flowchart of remaining fatigue lifetime determination of the of IGBT power modules

An electro-thermal model of the H-bridge converter will be implemented using PLECS toolbox so that by feeding the current profile into the model, the junction temperature of the IGBTs and diodes will be estimated. As mentioned before, the junction temperature is expected to have a very similar pattern to that of the current. Once the junction temperature is obtained Rainflow cycle counting will be performed on this irregular signal in order to identify regular cycles inside.

The lifetime characteristic of power modules that uses PrimePack packaging technology is available [8]. The characteristic is fitted with Coffin Manson law in order to find out a module-related coefficient. The resulting coefficient is used to estimate the number of cycles to failure corresponding to each temperature difference and mean temperature of the cycles identified with Rainflow analysis from the junction temperature profile.

The Palmgren Miner law considers that each stress cycles (in this case temperature) identified with Rainflow technique has a contribution on the overall damage and the damage accumulates linearly. By knowing the overall damage the remaining fatigue lifetime can be estimated (i.e. to how many repetitions of the loading history sequence can the power module be exposed to).

In order to make lifetime predictions three cases are simulated. The first simulation is performed with the received current profile at an arbitrary water temperature of $T_{\text{water}}=21^{\circ}\text{C}$. Afterwards, in order to check the influence of the chimney on the junction temperature and to see how it affects the lifetime of the power module the chimney will be removed.

As Coffin-Manson law takes into consideration also the effect of the mean temperature and in order to point it out, another simulation will be performed with an increased water temperature of $T_{\text{water}}=80^{\circ}\text{C}$. This scenario corresponds to the case when due to the degradation of thermal paste, the contact between baseplate and heatsink is not uniform anymore and the thermal resistance will increase.

1.5. Limitations

- Due to computational power limitations the model could not be verified by the use of the whole mission profile until failure. The thermo-electrical model requires long time to run and big resources, due to the fact that it performs many computations.
- The temperature of the water that it is used in the power cycling setup by Danfysik is unknown. An arbitrary value of $T_{\text{water}}=21^{\circ}\text{C}$ has been chosen for its normal operation and $T_{\text{water}}=80^{\circ}\text{C}$ to simulate the best and worst case scenarios.

2. System modeling

The lifetime of IGBT power modules depends strongly on the junction temperature. During normal functioning of the converter power modules are subjected to a high variation of the loading current that will generate junction temperature swings. These fluctuations stress the wire bonding and die-attach solder and lead to failure. Before looking into the recorded data of the real functioning conditions of power modules the converter behavior will be simulated and observed considering a repetitive constant pattern of the current. The purpose is to have an idea about the expected temperature that the power module will reach and its oscillations. Thus, in the following chapter an electro-thermal model for determining the power loss and junction temperature of the power module will be implemented using Simulink and PLECS toolboxes.

2.1. Converter principle of operation

The converter operates in quadrants I and IV, i.e. voltage may have both positive and negative polarity, while the current is only positive.

When T_1 and T_4 are switched on both the output voltage and current are positive. Power is taken from the source and fed into the load. This operation takes place in the first quadrant.

When T_1 and T_4 are switched off, the output voltage becomes negative and diode D_2 and D_3 are forward biased. The energy stored in the inductor will maintain the output current positive [4].

The conductive elements are indicated with red color in Figure 7:

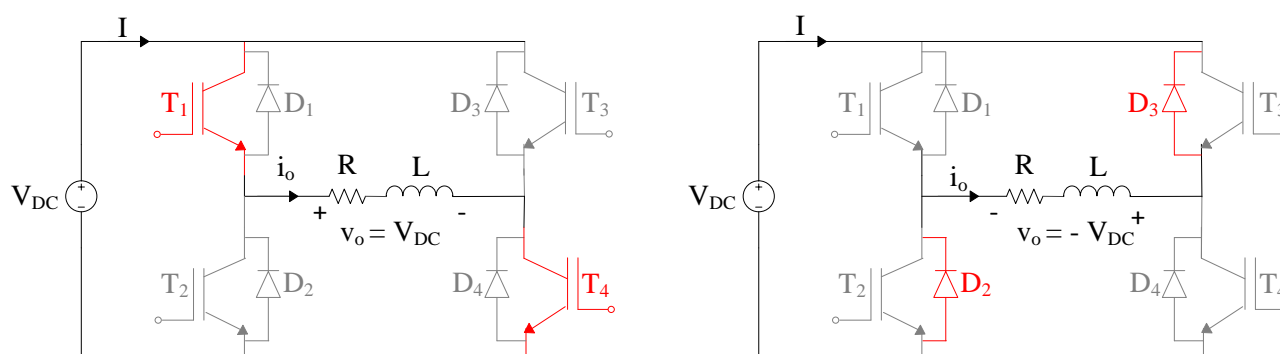


Figure 7 Operation of an H bridge converter in quadrant I and IV [4]

2.2. Converter modeling

The main steps for obtaining the junction temperature are presented in the flowchart depicted in Figure 8:

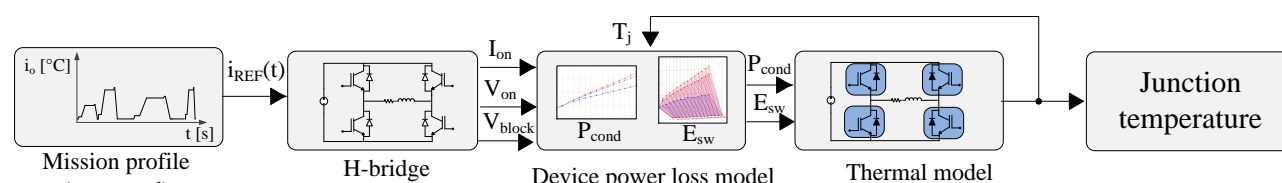


Figure 8 Flow chart of obtaining the junction temperature in PLECS

Each step from the flowchart will be described in the following sub paragraphs and finally the results will be presented.

2.3. Electrical circuit and controller design

The converter topology, function and parameters have been presented in the introduction and Section 2.1. The H-bridge was simulated using ideal components from PLECS toolbox. The switches are PWM controlled and the whole procedure of control is depicted in Figure 9:

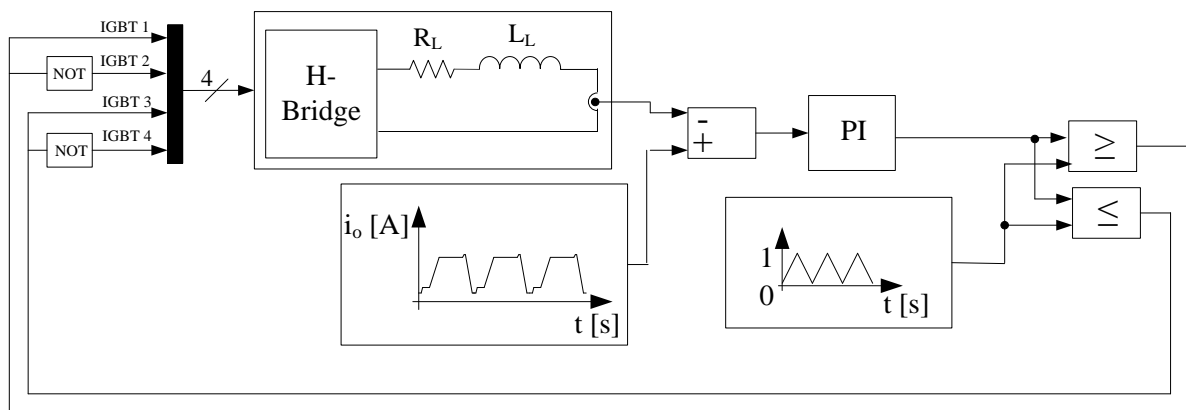


Figure 9 Closed loop control of the H bridge converter

The measured current from the RL load is compared against the current pattern presented in the introduction chapter. The resulted error is fed into a PI controller for minimising it and the output voltage signal is compared with a carrier signal in order to generate the PWM and fed it into the gates of the transistors.

The PI controller has been chosen in order to reach zero steady state error. When tuning the coefficients of the controller the same procedure was followed as in the case of the inner current control loop in control of electrical drives based on optimum modulus criterion [9]. This type of control is used for systems that have a dominant time constant and other minor time constants. Its purpose is to cancel out the dominant time constant and increase the speed of the system. The block diagram of the PI controller, an approximation of a delay introduced by the sampler, the gain of the inverter and the RL load is shown in Figure 10:

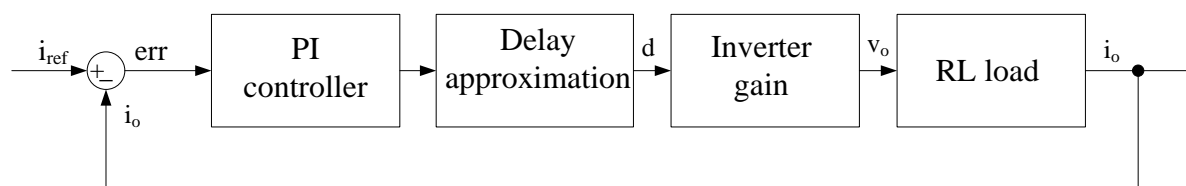


Figure 10 Block diagram of the H bridge converter

The transfer function of the PI controller is given by Eq. (2-1):

$$G_{PI}(s) = K_P + \frac{K_I}{s} = K_P * \left(\frac{1 + T_i * s}{T_i * s} \right) \quad \text{Eq. (2-1) [9]}$$

The delay is approximated to a time constant T_d equal to half of the switching period:

$$G_{delay}(s) = \frac{1}{1 + T_d * s} \quad \text{Eq. (2-2) [9]}$$

where:

$$T_d = \frac{1}{2 * f_{sw}} \quad \text{Eq. (2-3) [9]}$$

The RL load is modelled as a first order plant with the time constant: $\tau = L/R$:

$$G_{load}(s) = \frac{1}{R} * \frac{1}{1 + \tau * s} \quad \text{Eq. (2-4) [9]}$$

The open loop transfer function of the system is:

$$G_{OL}(s) = K_P * \left(\frac{1 + T_i * s}{T_i * s} \right) * \left(\frac{1}{1 + T_d * s} \right) * \left(\frac{1}{R} * \frac{1}{1 + \tau * s} \right) \quad \text{Eq. (2-5)}$$

In order to improve the system dynamic the slowest pole needs to be cancelled out by the zero of the PI controller, thus it is considered that: $T_i = \tau$ [9]. The open loop transfer function becomes:

$$G_{OL}(s) = \frac{K_P}{T_i * R_L} * \frac{1}{s * (1 + T_d * s)} \quad \text{Eq. (2-6)}$$

In order to ease the calculations all the constants are grouped together and the following notation is made:

$$T_c = \frac{T_i}{\frac{K_P * V_{DC}}{R}} \quad \text{Eq. (2-7)}$$

The open loop transfer function is:

$$G_{OL}(s) = \frac{1}{s * T_c * (1 + T_d * s)} \quad \text{Eq. (2-8)}$$

The closed loop transfer function may then be described by Eq. (2-9):

$$G_{CL}(s) = \frac{G_{OL}(s)}{1 + G_{OL}(s)} = \frac{\frac{N}{D}}{1 + \frac{N}{D}} = \frac{N}{D + N} \quad \text{Eq. (2-9)}$$

Where N=nominator and D=denominator of a transfer function in general.

The closed loop transfer function is then:

$$G_{CL}(s) = \frac{1}{T_c * T_d * s^2 + T_c * s + 1} \quad \text{Eq. (2-10)}$$

An analogy with the standard form of a second order transfer function from Eq. (2-9) is made in order to identify the K_P , K_I , the undamped natural frequency and damping factor of the system:

$$G_{CL}(s) = \frac{1}{\left(\frac{s}{\omega_n} \right)^2 + 2 * \xi * \frac{s}{\omega_n} + 1} \quad \text{Eq. (2-11) [10]}$$

The undamped natural frequency and the damping factor are found as:

$$\omega_n = \frac{1}{\sqrt{T_c * T_d}}; \frac{2 * \xi}{\omega_n} = T_c \rightarrow \xi = \frac{1}{2} * \frac{T_c}{\sqrt{T_c * T_d}} = \frac{1}{2} * \sqrt{\frac{T_c}{T_d}} \quad \text{Eq. (2-12)}$$

From the condition:

$$\xi = \frac{\sqrt{2}}{2} \rightarrow T_c = 2 * T_d = \frac{T_i}{\frac{K_P * V_{DC}}{R}} \quad \text{Eq. (2-13) [10]}$$

By inserting Eq. (2-12) in Eq. (2-13) the proportional gain is found to be:

$$K_P = \frac{\tau * R_L}{2 * T_a} \quad \text{Eq. (2-14)}$$

Thus, the values of the proportional and integral coefficients are:

$$K_P \cong 6 \text{ and } K_I = \frac{K_P}{T_I} \cong 5 \quad \text{Eq. (2-15)}$$

The design of the PI controller has been considered only for the particular case of $R=0.112$ [Ω] and $L=0.135$ [H]. Tuning it for other working points is out of scope of this project.

The Bode diagram of the open loop system and the time response for a step input are shown in Figure 11 and Figure 12:

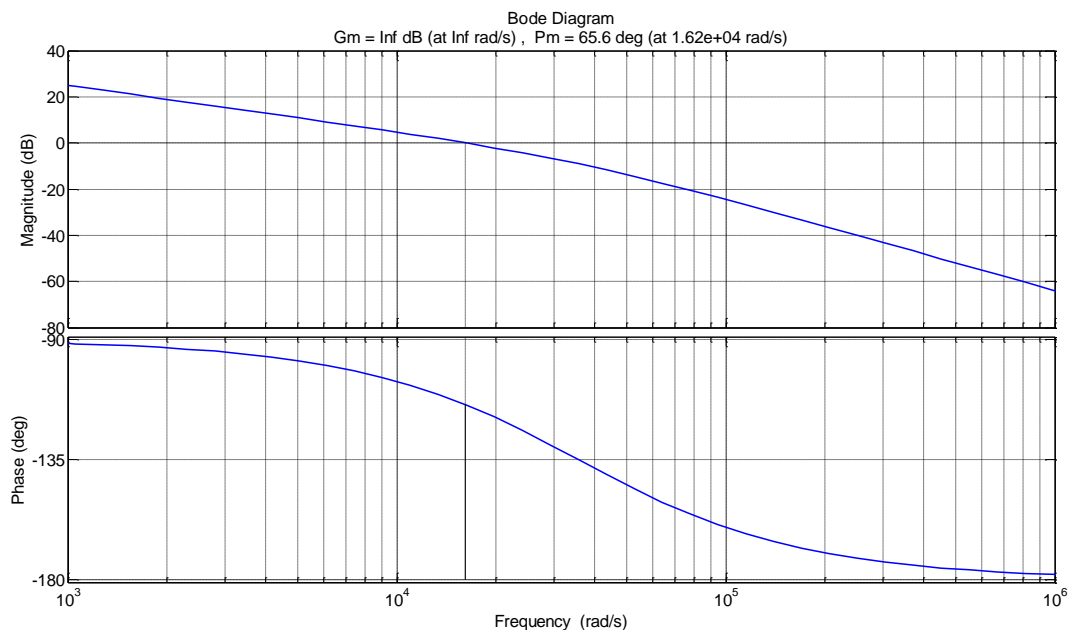


Figure 11 Open loop Bode diagram of the system

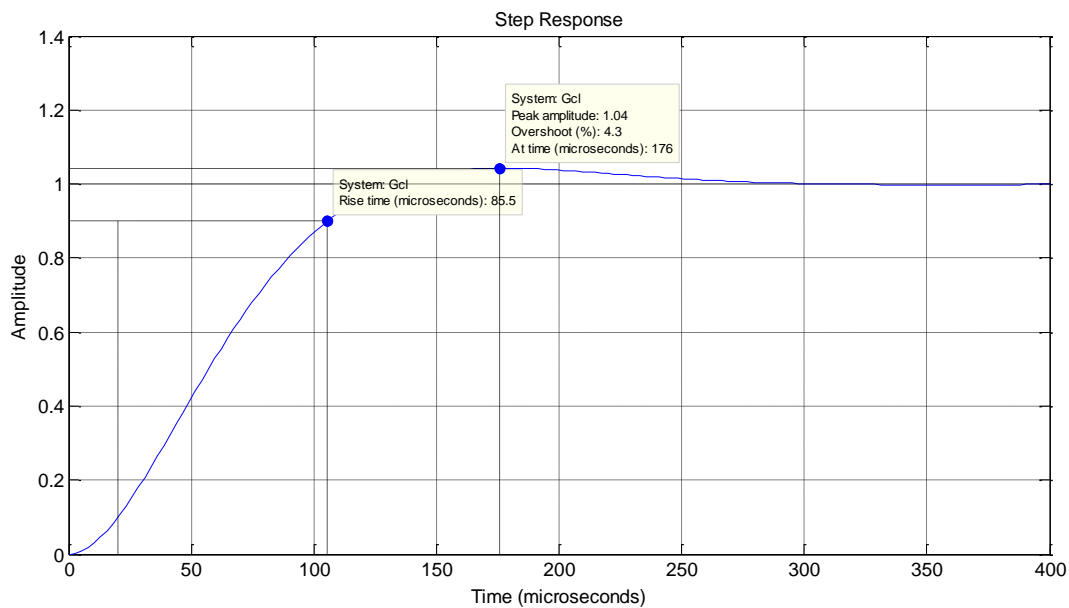


Figure 12 Time response to a step input of the system

From the Bode plot of the open loop system it can be seen that the phase margin is 65.5° and the gain margin is infinite indicating that the closed loop system is stable. From the time response to a step input the system has been observed to have a maximum overshoot of 4.32 %, time of the maximum overshoot at 176 [us] and the settling time using the 2% criteria [10] as 237[us].

2.4. Power loss model

Conduction losses:

The simulation has been performed using PLECS toolbox. The choice is justified by the ease in modelling, as PLECS is using ideal components and parameters offered in the datasheet of the component. Also it is computationally faster.

Forward characteristics at different junction temperatures were inserted in a look-up table. The characteristics are presented in the datasheet of Appendix A.

It has the form of a structure with the on-state current and temperature as index vectors and it outputs matrix v [11] . PLECS is performing linear interpolation between the points automatically. During each simulation time step the conduction loss is calculated by the product of the on-state voltage and on-state current and it interpolates in case of intermediate points. (first order interpolation)

The conduction losses curves of the IGBT chip and diode are depicted in Figure 13. All the data points that were inserted in the thermal description of the IGBT and diode can be found in tables in Appendix B.

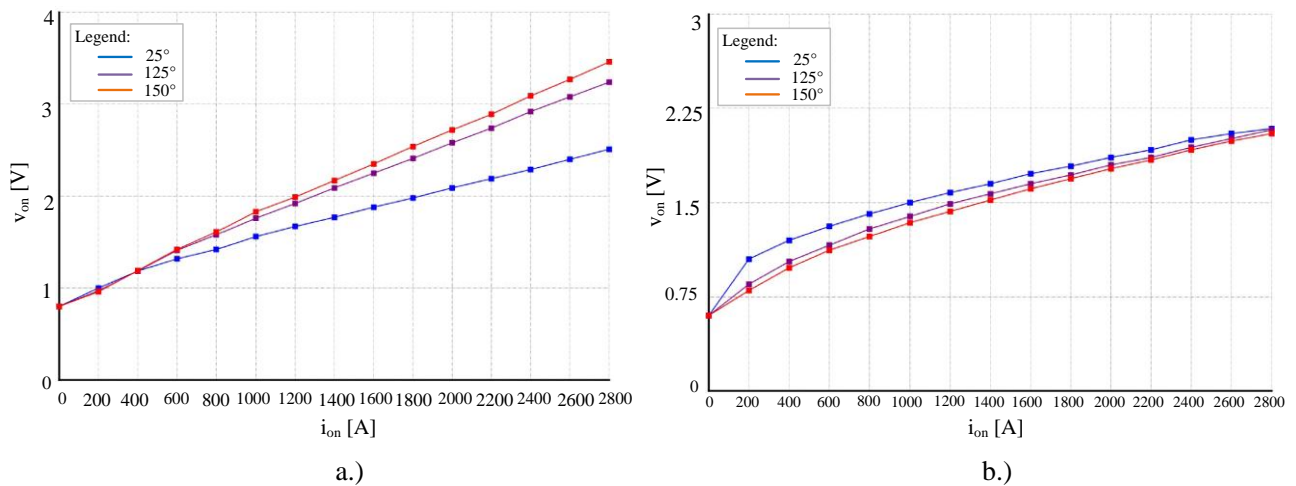


Figure 13 Conduction power losses: a.) of IGBT; b.) of the diode

In a similar manner, for calculating the switching losses of a semiconductor device, points from the curves illustrating the energy consumption during switching with respect to blocked voltage, forward current and T_j , are used. The points are fitted in a look-up table and represented by PLECS using energy surfaces. The look-up table contains three index vectors as the blocked voltage, on-state current and device temperature and it outputs the switching energy loss in [mJ].

However, the datasheet of the power module does not offer any information regarding the conduction and switching power losses at 25°C. In order to obtain positive values for the losses an approximation had to be done. When calculating power losses PECS interpolates/extrapolates linearly to get the value corresponding to a certain temperature value. For small switching losses at 25°C by linear interpolation the interpolated value was negative.

A vector of values with interpolated energy switching losses has been calculated:

$$E_{150} - E_{125} = x \quad \text{Eq. (2-16)}$$

Then instead of going 4 times down to 25°C, since the on state current-on state voltage dependence is exponential and not linear a rough approximation with a coefficient of ‘2.5’ has been used to find out the desired values:

$$E_{25} = E_{125} - 2.5 * x \quad \text{Eq. (2-17)}$$

x represents the point that results from the difference between the energy loss at 150°C and energy loss at 125°C: The results were checked against the datasheet plots and were the same.

The switching losses of the IGBT are depicted Figure 14. The off state losses of the diode are depicted in Figure 15:

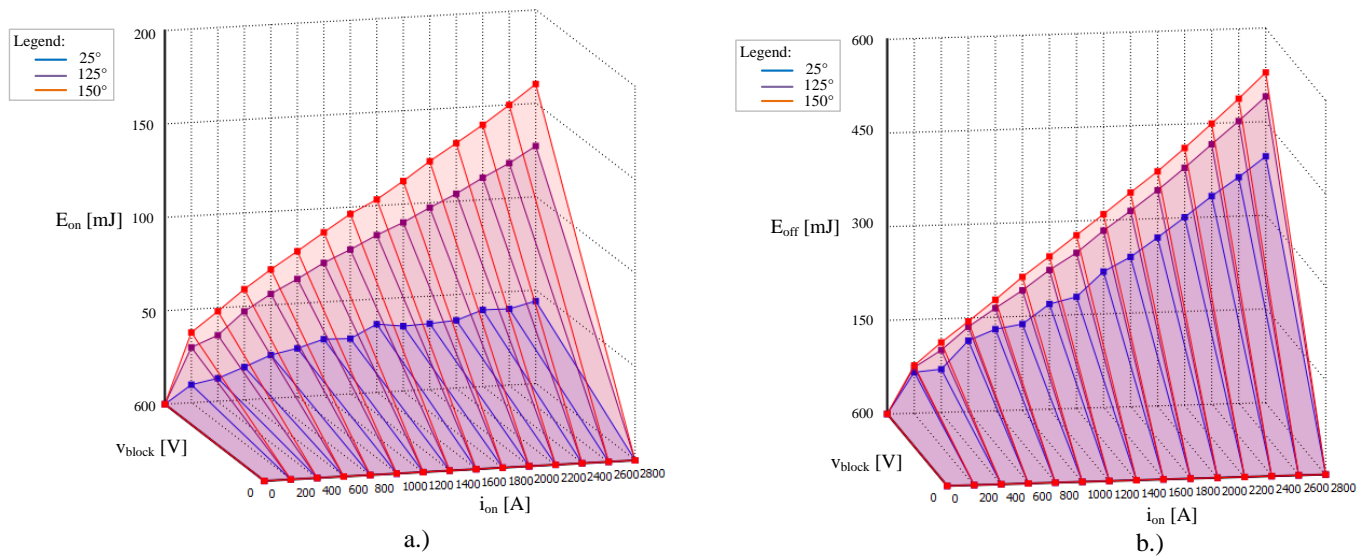


Figure 14 Switching power losses of IGBT: a.) On state; b.) Off state

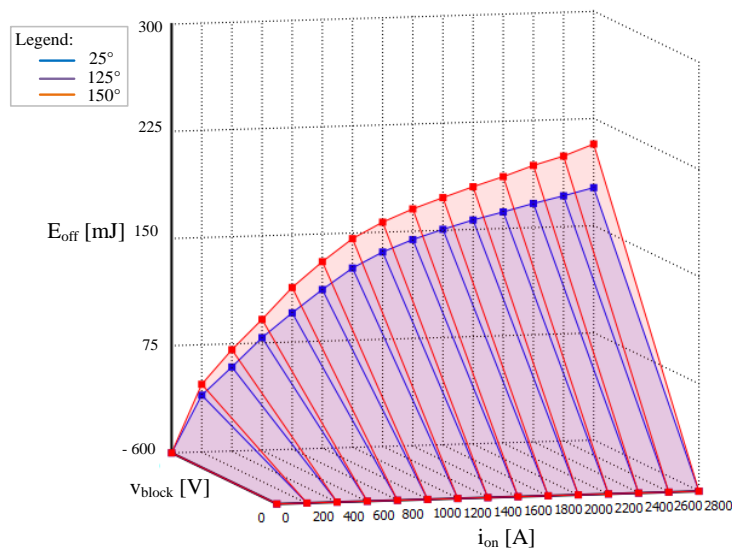


Figure 15 Off state energy loss of the diode

2.5. Thermal modelling of IGBT power modules

Thermal behaviour of semiconductor components may be described using RC circuit models based on the analogy between electrical and thermal domains. One solution is to use Foster model circuit due to accessibility. The circuit includes parallel RC elements and thermal coefficients for the Foster model that are usually provided in the datasheet by the manufacturer. As it can be seen in Figure 16 in the box placed in the right bottom corner the values of the thermal resistances and thermal time constants are given for both IGBT and diode:

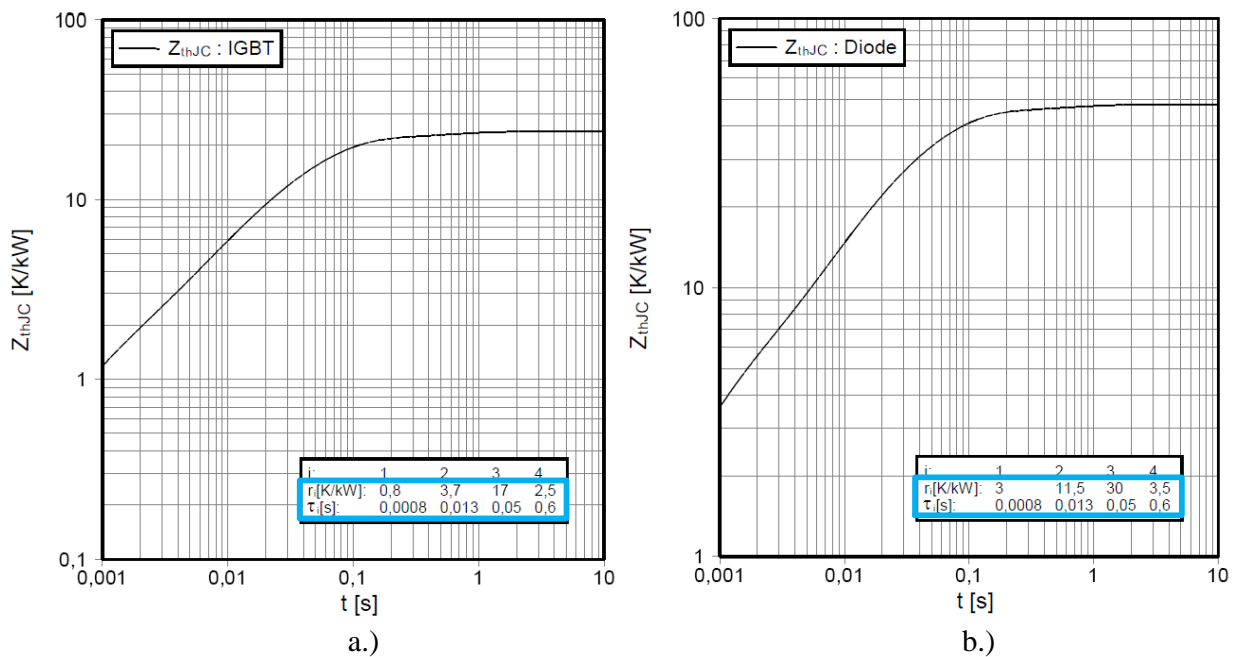


Figure 16 Thermal impedance variation with time: a.) for IGBT; b.) for diode [5]

However, the analysis based on Foster network represents only a mathematical model and the circuit nodes have no physical meaning. Thus, it does not allow access to internal temperatures of different component layers. Another option is the use of Cauer models. These networks have a physical meaning and temperatures of component layers may be found out. It requires knowledge about the internal structure of the power module and since that was not possible and the Foster parameters of the cooling system were provided, the Foster network will be further used in modelling.

Thermal capacitances are extracted from the thermal time constants according with Eq. (2-18):

$$C_{thi} = \frac{\tau_i}{R_{thi}} \quad \text{Eq. (2-18) [12]}$$

The representation of the Foster network with the thermal parameters from the datasheet is depicted in Figure 17. The power loss [W] that is fed into the thermal circuit (for the IGBT/diode) is equivalent to the current in electrical domain [A]. The main difference is that power loss flow is unidirectional. The thermal resistances are found in the datasheet as previously indicated and the thermal capacitances are calculated by using Eq. (2-18):

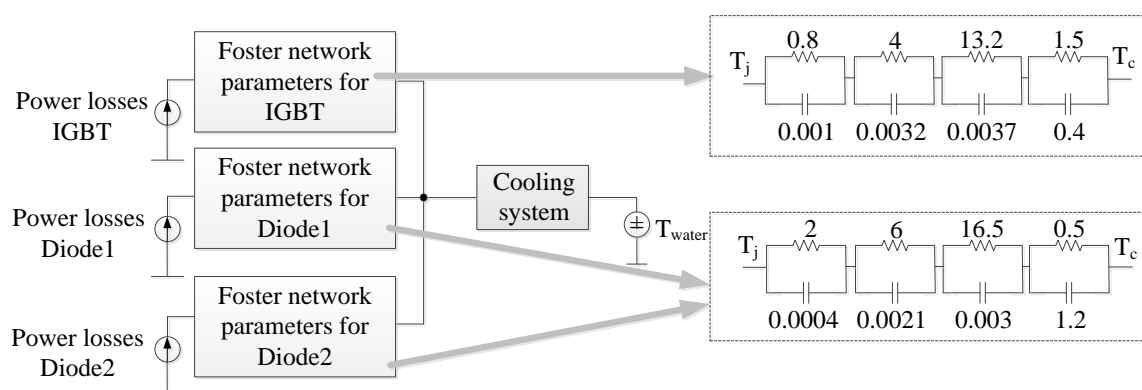


Figure 17 Foster representation of IGBT/diode

The connection between the electrical and thermal domain in PLECS is made through the heat sink. In PLECS it is represented by a blue square like in the block diagram from Figure 18. It absorbs the losses of the components contained inside its boundaries and feeds them into the thermal model [11]. Since the cooling system is more complex and contains thermal coefficients not only for the aluminium heat sink, but also for the thermal paste and water cooling, the heat sink is further connected to an equivalent RC Foster network. The thermal parameters were provided by Danfysik.

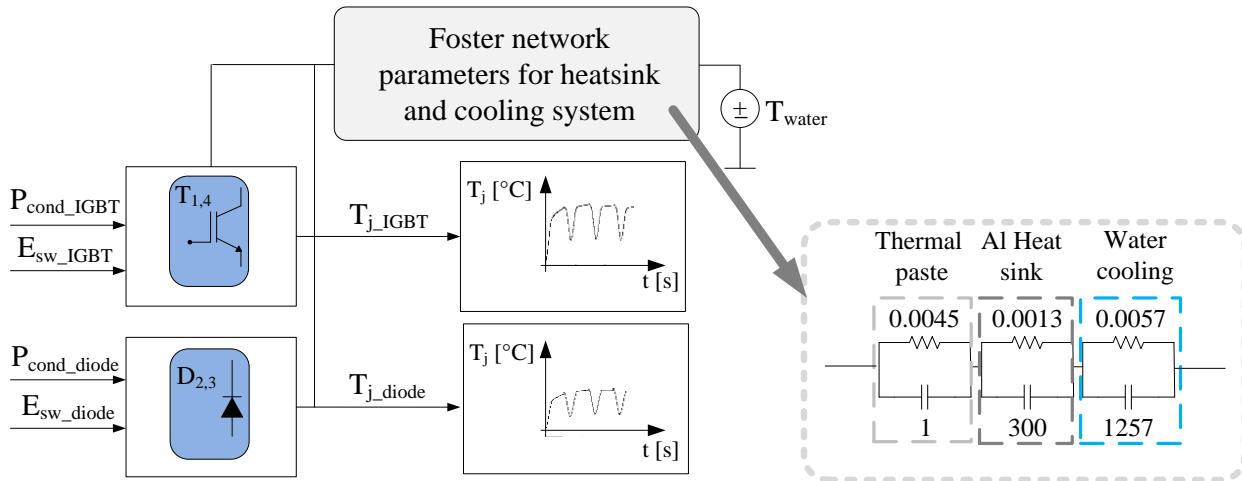


Figure 18 Block diagram of thermal model implementation in PLECS

Afterwards, the new calculated junction temperature is updated into the loss model for the next iteration of the power losses as it was indicated in the flowchart from Figure 8.

In the simulation an arbitrary ambient temperature of 21°C has been considered. All the Foster parameters included in the simulation may be found in Appendix B.

2.6. Simulation results

The simulation model had been verified by applying a repeating sequence of the current pattern presented in the introduction.

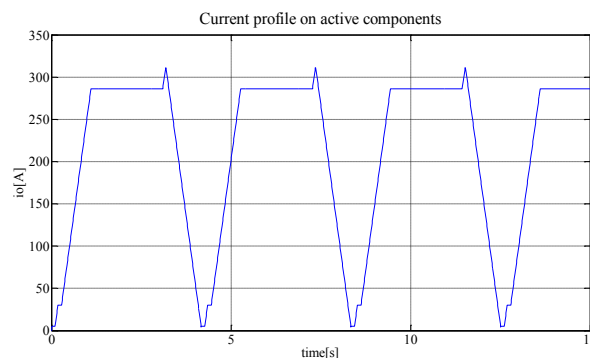


Figure 19 Current waveform on active components

The current sequence is about 4.5 times smaller than the nominal current $I_{C_{nom}}$ (Table 2), so the temperature is not expected to raise much towards maximum temperature. As it can be seen in Figure 20 and Figure 21 on the first leg the most stressed component is IGBT1, followed by D_2 . It

confirms that the model is working according to the functioning description of the H-bridge as presented in Section 2.1.

The temperature of the IGBT rises up to 55°C and it is increasing, while in the case of the diode the temperature goes up to 34°C and due to the cooling system it is starting to decrease. The difference in temperature for the IGBT is about 22°C and 17°C for the diode. The temperature shape is following more accurately the shape of the current in the diode case, but as it can be seen in all the cases the spike of the current influences the temperature shape. The influence of the current spike on the components will be studied in the next chapter.

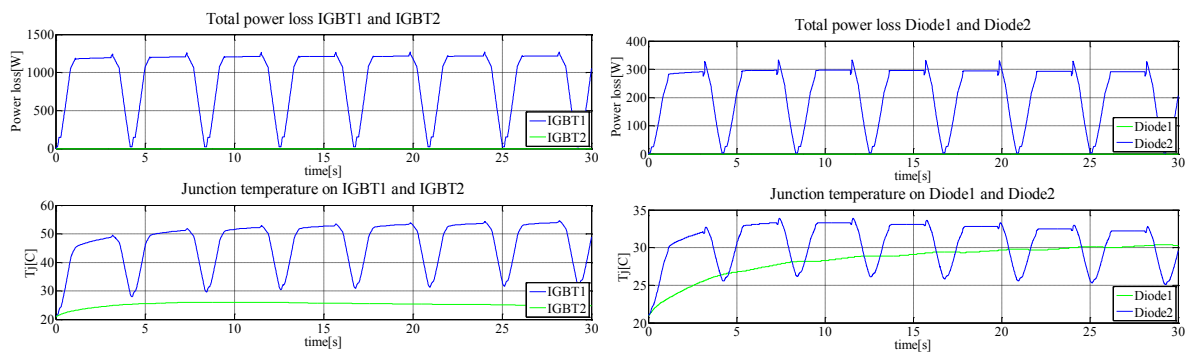


Figure 20 Total power loss and junction temperature on first leg elements

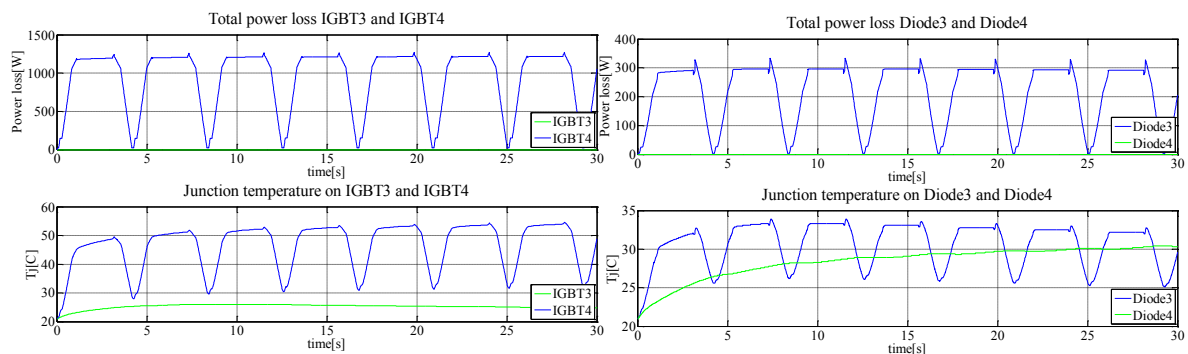


Figure 21 Total power loss and junction temperature on second leg elements

2.7. Summary

The characteristics and functioning of an H bridge converter has been described and an electro-thermal model has been developed using PLECS toolbox for simulating it. The model has been validated for a repeated type of ramp current shape and the thermal behaviour of the converter has been analysed.

3. Lifetime modelling

When dealing with an irregular junction temperature variation a cycle counting method should be used. Its role is to make possible the comparison between variable loading data test and constant amplitude test, all the estimation available data found in literature being for constant amplitude.

In this chapter Rainflow cycle counting will be used in conjunction with Coffin Manson law that models the fatigue of the bonding wires and solder. To calculate how much the temperature is stressing the power module Palmgren Miner will be used. These steps will be applied on the scenarios specified in the Introduction chapter.

One of the most popular cycle counting methods is the Rainflow technique. This method identifies regular ranges within an irregular signal and eliminates the smaller ones first. Afterwards, the obtained temperature ranges are compared with available data for constant amplitude loading, i.e. the lifetime characteristic of the power modules for this case. By the use of Palmgren Miner linear damage rule the damage each temperature cycle produces on the power module is quantified. The whole procedure is summarized in the flowchart depicted Figure 22:

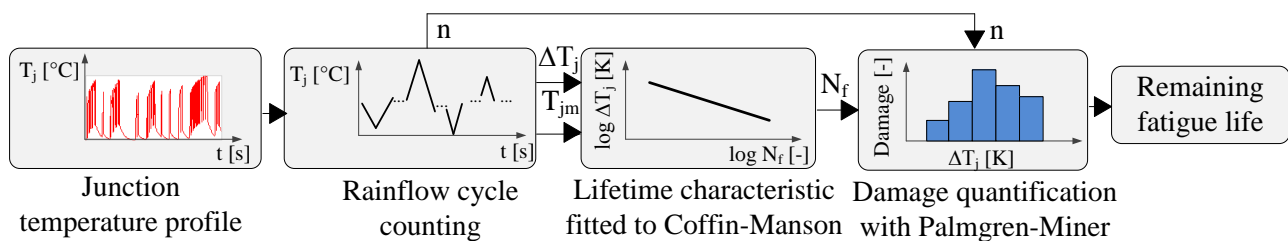


Figure 22 Flowchart of remaining fatigue lifetime estimation

3.1 Rainflow cycle counting method

The programme for Rainflow counting method is provided on Mathworks website [13]. Before the Rainflow counting technique is applied, the local extrema of the signal have to be identified. This is done by using the function sig2ext.m that is included on the attached CD. For example, a fictitious junction temperature signal on a semiconductor is considered in Figure (top). The extrema on every cycle are identified next in Figure (bottom):

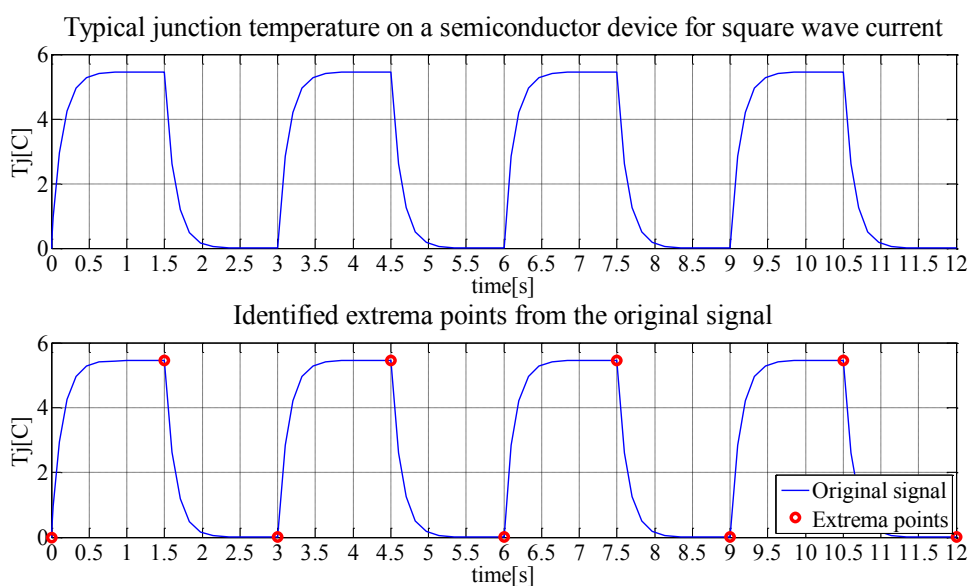


Figure 23 Identification of the extrema from a regular junction temperature profile in Matlab

There are more types of Rainflow algorithms, but their results are similar [14]. The one that will be used and described within this project is the three point check due to the fact that it is simple and computationally fast.

The three point counting algorithm checks three consecutive points to determine if a cycle is formed or not. The low amplitude cycles are separated from the high amplitude ones. When a cycle is counted it is discarded and the remaining points are connected together. The remaining residue is counted until all the points are exhausted. The two rules of the algorithm are the following [14]:

- If $X \geq Y$ and point P_1 is not the starting point of the loading history, then a cycle is counted and both P_1 and P_2 are discarded.
- If $X \geq Y$ and point P_1 is the starting point of the loading history, then a reversal or half-cycle is counted from P_1 to P_2 , and only P_1 is removed.

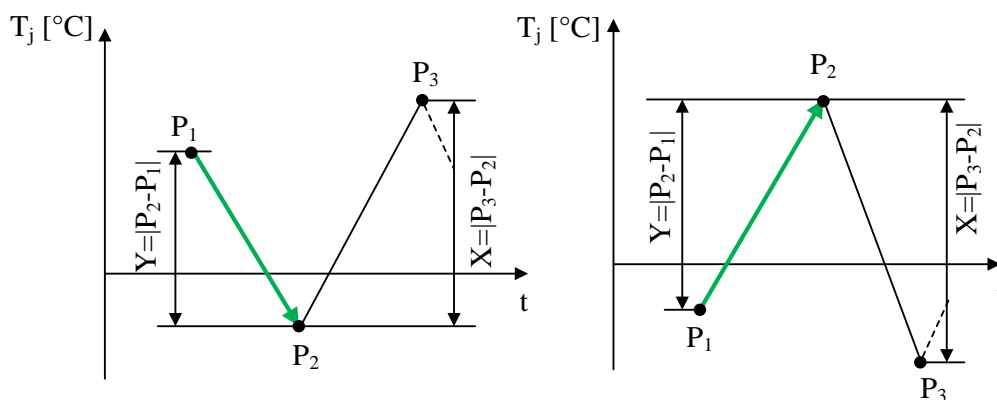


Figure 24 Three point counting method: extracting half cycles at the starting points and counting a half cycle from P_1 to P_2 [14]

In the given example from Figure 23 all the segments of the signal are equal. In Figure 25 only half of the time history is shown to give an idea about how the cycles are counted. The rules apply in the same manner until the end of the load history:

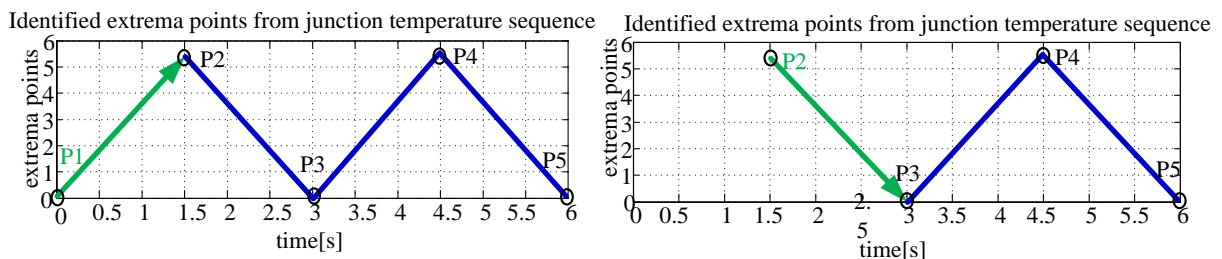


Figure 25 Rainflow cycle counting technique applied on the sequence of extrema

The first segment is considered under the first rule: the range $|P_3 - P_2|$ is equal to $|P_2 - P_1|$ and P_1 is the first point of the loading history, so only P_1 is discarded and a half-cycle is counted. The counting is continued for the range $|P_4 - P_3|$ that is equal to $|P_2 - P_3|$. A half-cycle is counted from P_2 to P_3 and again, P_2 is the first point in history and gets discarded. In total 8 half-cycles are counted.

The signal with the identified extrema is shown in Figure 26 (top). The function `rfdemo1.m` shows how the counting is performed in Matlab in a graphical matter as depicted in Figure 26 (bottom). The half-cycles are marked by coloured sine waves and text that indicates the direction of the counting.

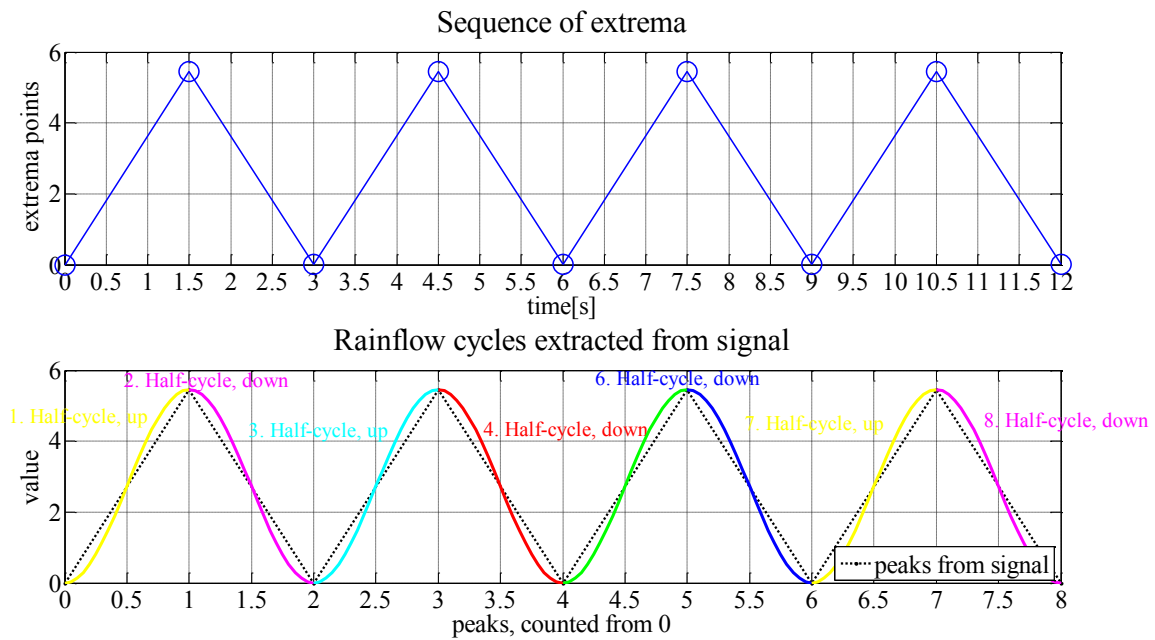


Figure 26 Rainflow cycle counting technique performed in Matlab on the sequence of extrema

After the cycles are identified, their amplitude s (or ranges) and mean values are stored in a matrix. The Rainflow matrix contains also a row with a value of 1 for the identified full cycles and 0.5 for half cycles.

If the loading profile is an irregular one then after finding the extrema the signal may look like the one in Figure 27. The main parameters of any time history are calculated as it is indicated in the picture. Two arbitrary points, P_1 and P_2 are taken as an example in the zoomed-in part of the figure:

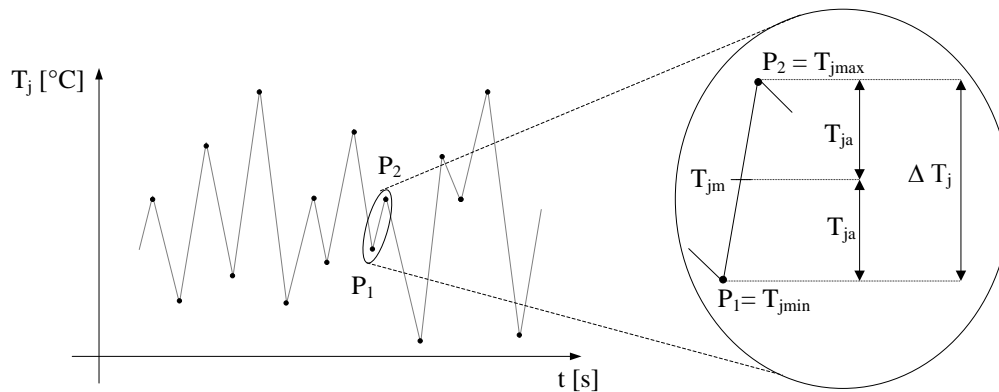


Figure 27 Parameters of an irregular temperature loading

The amplitude of an identified cycle is found using the formula:

$$T_{ja} = \left| \frac{T_{jmax} - T_{jmin}}{2} \right| \quad \text{Eq. (3-1) [15]}$$

Its mean value is:

$$T_{jm} = \frac{T_{jmax} + T_{jmin}}{2} \quad \text{Eq. (3-2) [15]}$$

The range of the identified cycle is defined as:

$$\Delta T_j = |T_{j\max} - T_{j\min}| \quad \text{Eq. (3-3) [15]}$$

The ranges of temperature from the ‘typical’ junction temperature profile considered in the example are the same and equal to $\Delta T = 5.45$ and the mean temperature of each half-cycle counted is $T_m = 2.72$.

3.2. Coffin Manson law

Among lifetime models the Coffin Manson law for plastic fracture is the most commonly used. It gives a mean value of the number of fatigue fracture of metals as a function of the change in temperature during each cycle [16].

In this project the modified equation that considers besides the junction temperature range also the mean temperature will be used:

$$N_f = A * (\Delta T_j)^\alpha * \exp\left(\frac{E_a}{k_b * T_{jm}}\right) \quad \text{Eq. (3-4) [3]}$$

where

N_f – number of cycles to failure [-]

A – constant [$K^{-\alpha}$]

ΔT_j – temperature range as described by Eq. (3-3) [K]

α – constant; $\alpha = -5.039$ [-] [16];

k_b – Boltzmann constant; $k_b = 1.38066 * 10^{-23}$ [J/K] [16];

E_a – activation energy; $E_a = 9.89 * 10^{-20}$ [J] [16];

T_{jm} – average temperature [K]; can be described also as $T_{jm} = T_{j\min} + \frac{\Delta T_j}{2}$

A is a constant that differs from module to module. The datasheet of the power modules does not include a lifetime curve, so a fitting has been done according to [16]. The purpose of the fitting is to find the value of constant A that has been identified as $A = 3.3125 * 10^6$. The plot from Figure 28 was verified experimentally for the IGBT [16]. The source mentions that the model for the diode should be the same for the case of the diode by the authors conversation with Infineon, but the model could not be verified experimentally.

The fitted curved using Ezyfit toolbox is depicted in Figure 28:

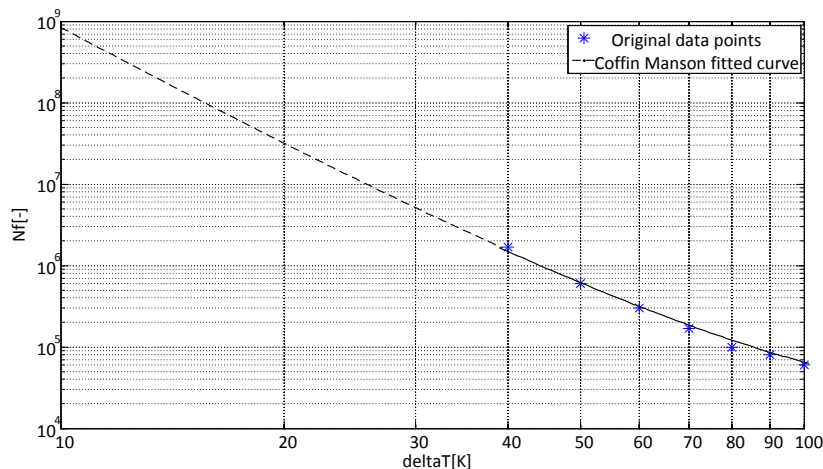


Figure 28 Expected number of cycles to failure as a dependence of the change in temperature obtained through curve fitting [16]

3.3. Damage modelling

Computation of the fatigue damage caused by the considered loading interval T_0 is usually realized with the assumption of hypothesis of linear fatigue accumulation. The used method is Palmgren-Miner rule which considers the damage as a fraction of life used by an event or a series of events [17], [18].

Total damage can be expressed as the sum of particular damages caused by each cycle:

$$D = \sum_{i=1}^j D[i] \quad \text{Eq. (3-5) [17]}$$

Where j is a number of cycles determined from the loading history using Rainflow cycle counting algorithm.

The particular values of damages D_i are determined for each cycle or half-cycle:

$$D = \frac{n[i]}{N_f[i]} \quad \text{Eq. (3-6) [17]}$$

for $i=1 \dots j$.

- n_i is the number of identified temperature cycles (equal to 1 for a cycle and 0.5 for a half-cycle)
- j is a number of cycles and half-cycles distinguished from the history
- N_{fi} is a number of cycles to failure computed with Coffin-Manson law (Eq. (3-4))

Thus, total damage is computed as:

$$D = \sum_{i=1}^j \frac{n[i]}{N_f[i]} \quad \text{Eq. (3-7) [17]}$$

These fractions are summed up and when their sum equals $D = 1$ or 100%, failure is expected and predicted (no damage failure means $D < 1$) [18].

3.4. Lifetime estimation

The expected lifetime of an object may be calculated from the damage caused by the identified cycles in the interval T_0 of the time history:

$$L = \frac{T_0}{D} \quad \text{Eq. (3-8) [17]}$$

3.5. Simulation results

By feeding an irregular current load history of 13408s length (about 3h 44m) that was provided by Danfysik into the model the thermal behaviour of the IGBT and diodes on the first leg has been observed. On the second leg the situation is mirrored considering the principle of operation of the H-bridge (as it was shown in the previous chapter).

A part of the current profile can be seen in Figure 29:

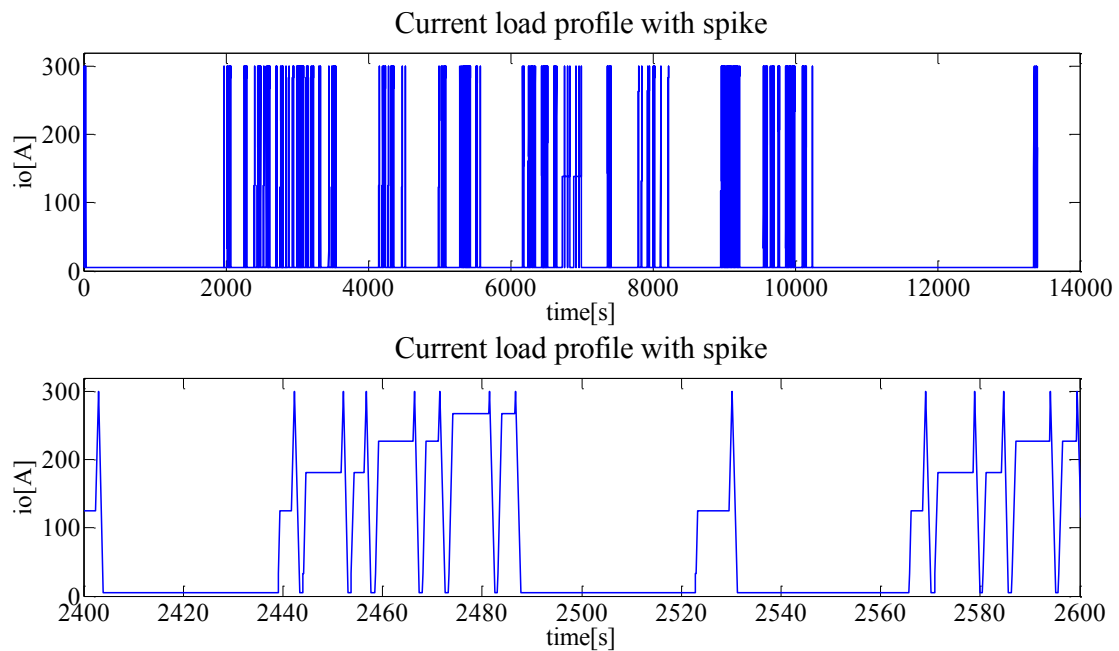


Figure 29 Irregular current loading history

From the load history in Figure 29 it can be observed how the current profile looks like. It has some intense time periods with low frequency ramps, followed by long breaks. The junction temperature on IGBT1, Diode 1, IGBT2 and Diode2 is depicted in Figure 30:

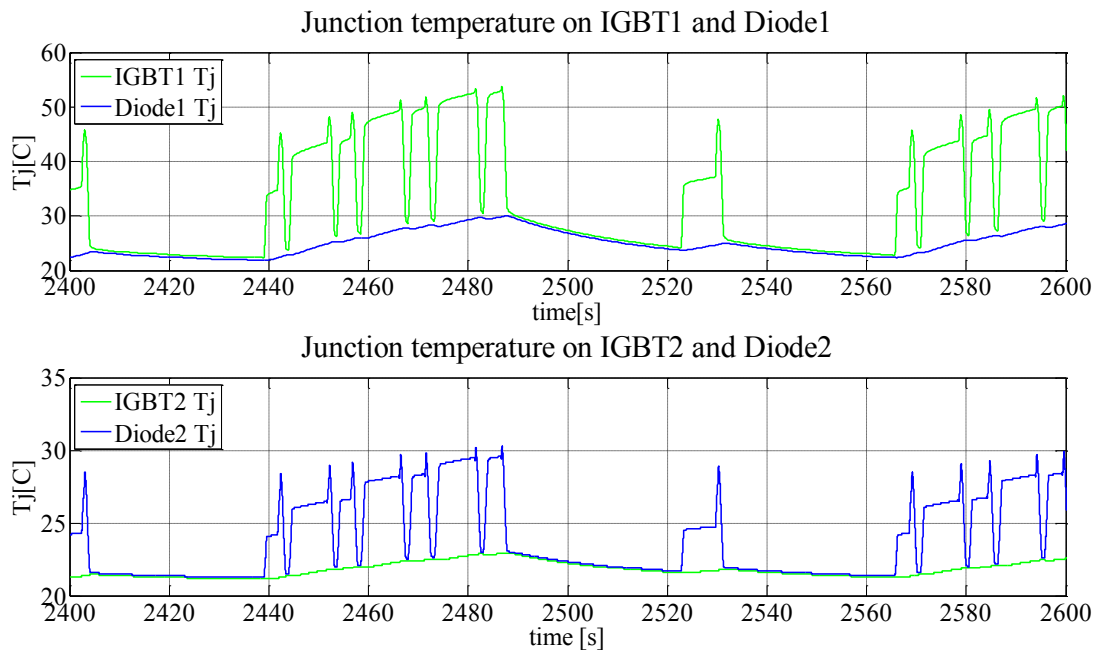


Figure 30 Junction temperature profile on IGBT1, Diode1, IGBT2 and Diode2

Afterwards, Rainflow cycle counting has been performed in order to identify temperature cycles inside the components temperature profiles as explained in Section 3.1. An example of how the counting is performed is given at the end of the project in Appendix C.

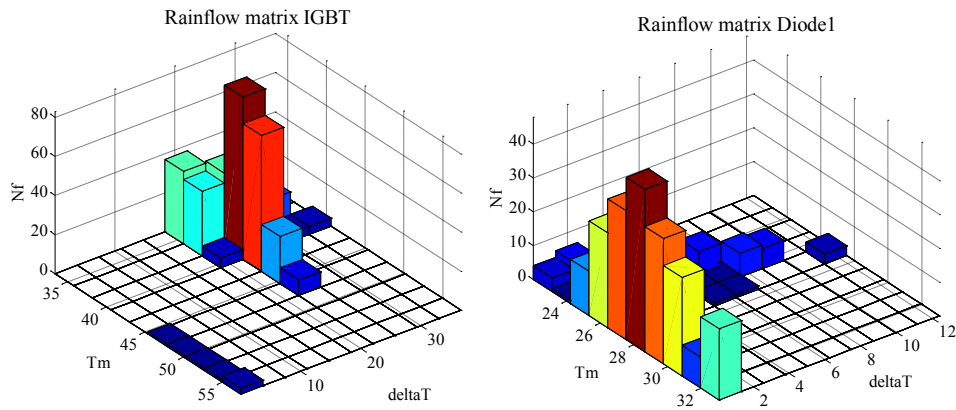


Figure 31 Rainflow 3D matrix showing the distribution of temperature ranges and average temperature among the counted cycles for IGBT1 and Diode1

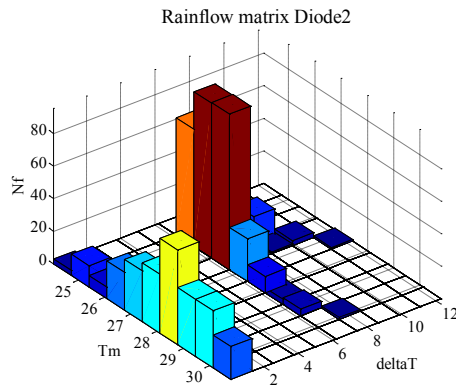


Figure 32 Rainflow 3D matrix showing the distribution of temperature ranges and average temperature among the counted cycles for Diode2

IGBT₂ case has not been considered anymore. The reason behind it is that as it can be seen in Figure 33 T₁-D₁-D₂ and T₄-D₄-D₃ are forming 2 IGBT power modules. T₂ and T₃ not used and they get heated up only by the heating of the water.

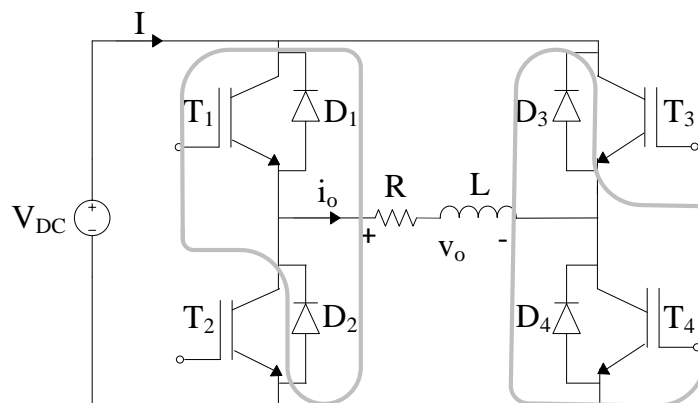


Figure 33 Resemblance of power modules inside the converter

As the situation is exactly the same for T₄-D₄-D₃ but mirrored, only the first leg will now be considered in analysis without T₂.

Next step was to quantify the damage on the components of the power module. The Rainflow histogram and the damage histograms of IGBT1, Diode1 and Diode 2 are shown in:

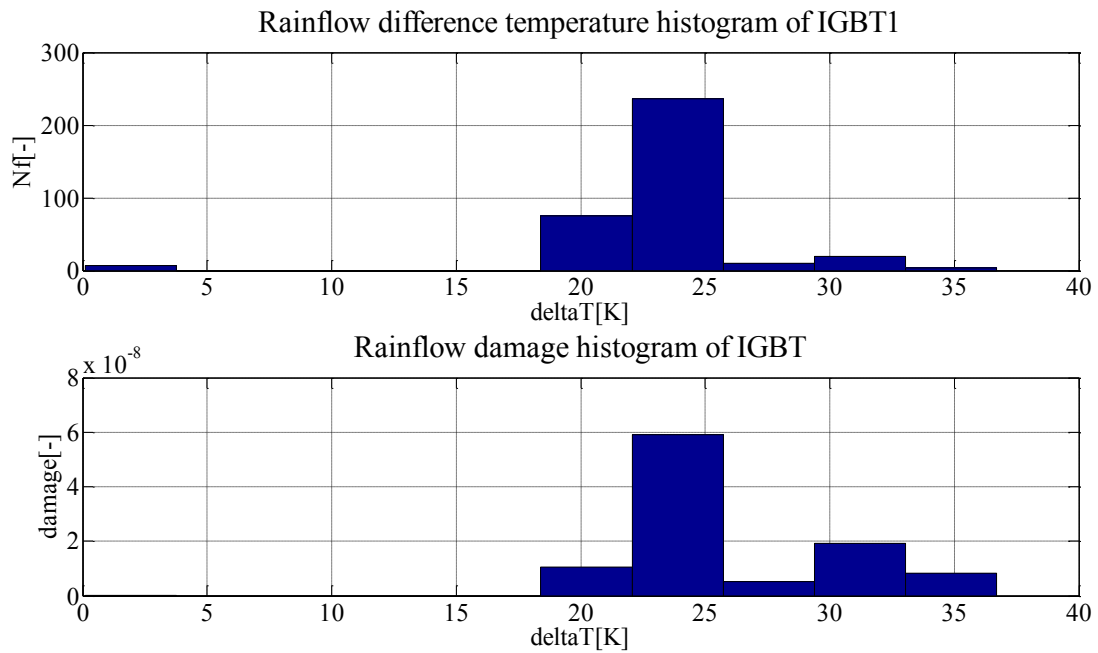


Figure 34 Damage histogram of IGBT1

As it can be seen in Figure 34 the temperature differences are not very different among cycles. Most of them have a ΔT of about 22° - 25° and only few for higher differences. However, the higher ranges affect more the IGBT than the smaller ones, as it can be seen in the damage histogram.

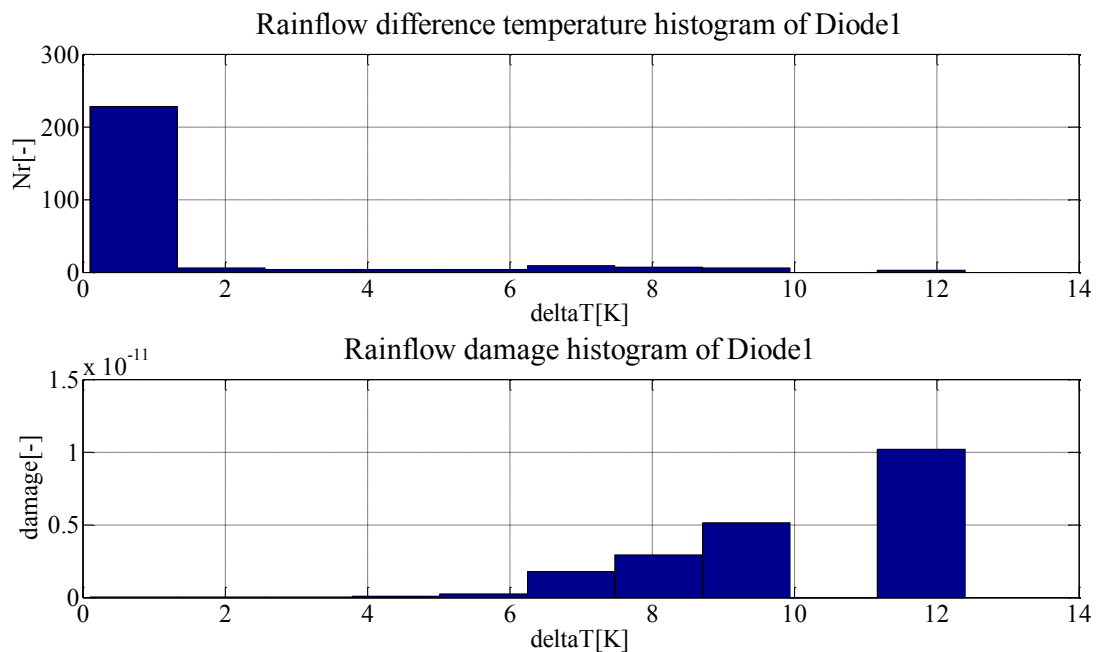


Figure 35 Rainflow histogram of the difference in temperature among counted cycles and the produced damage for Diode1

Diode 1 is not used at any instance, so it gets heated up only by the heating of water. The cycles have very low temperature differences, but as in the case of IGBT the higher ones are producing most of the damage.

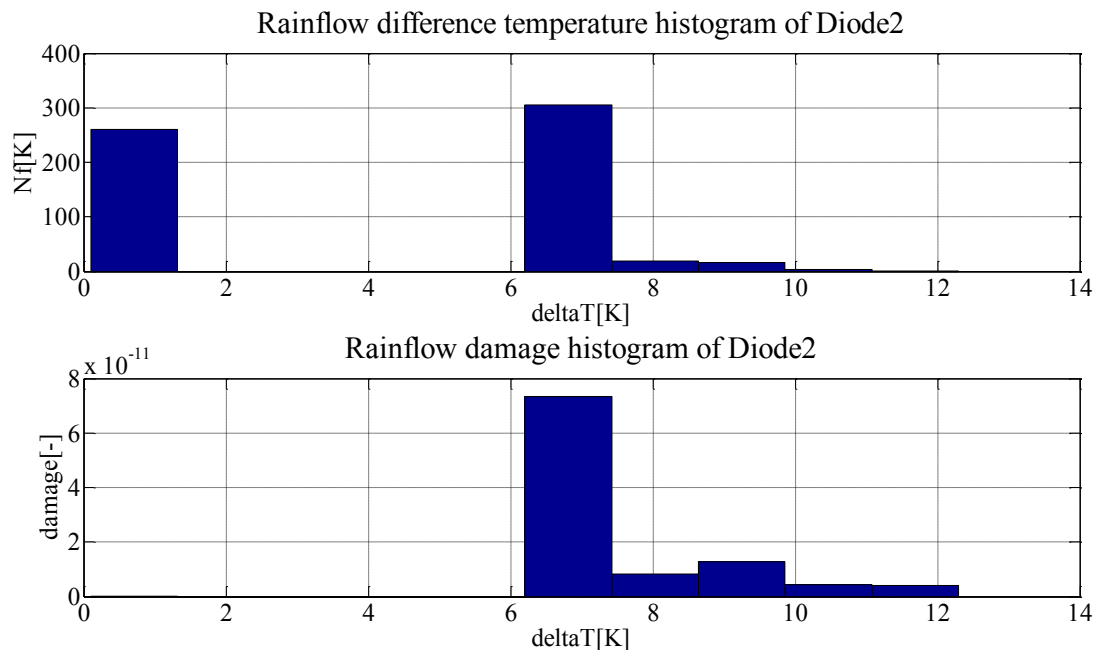


Figure 36 Rainflow histogram of the distribution of difference temperature among the counted cycles and the damage produced on Diode2

As expected the small cycles of ΔT have small contribution into the damage histogram, whereas the cycles with a higher difference in temperature are affecting more the components also for the case of Diode 1.

Estimations have been made as presented in Section 3.4 and the results show that the IGBT is the most affected component inside the power module experiencing higher differences in temperature. It can stand about 4 000 years of repetition of the sequence.

Diode1 is the least affected and it is estimated to be able to function under the repetition of the sequence 20 mill years.

Diode 2 is more stressed than Diode1 and the prediction for it is 4 mill years.

In order to check the influence of the spike it has been removed from the current profile and the resulted ramps have been fed into the electro-thermal model to observe the behaviour of the components.

A part of the current profile is depicted in Figure 37:

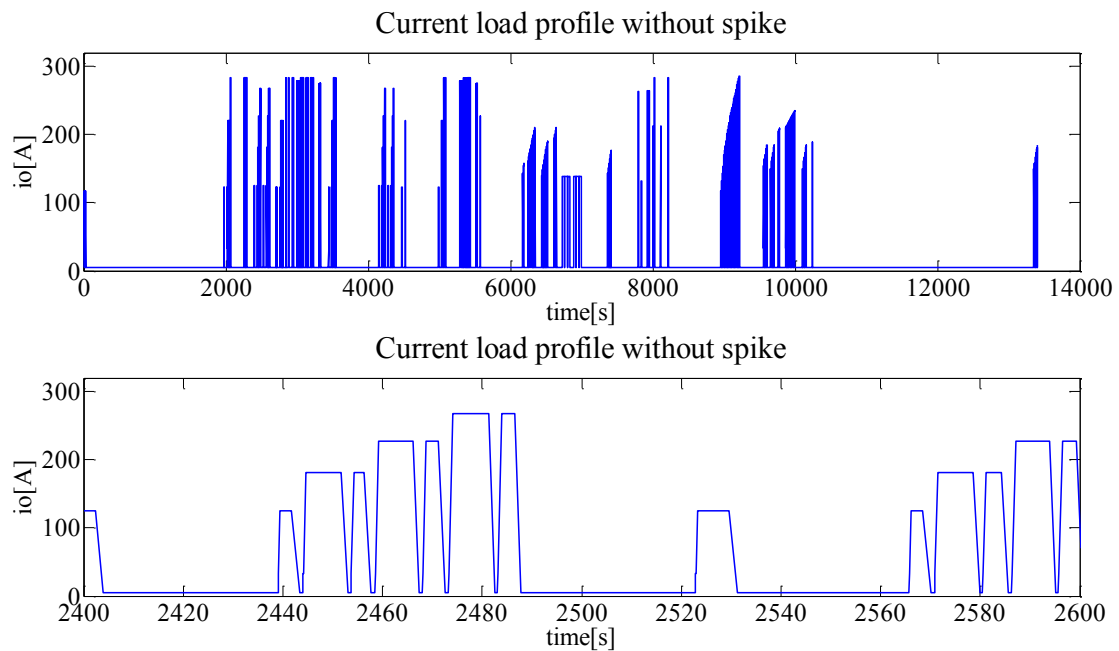


Figure 37 Current profile with the 'chimney' removed

The resulted current profile has lower amplitude and the situation is the same for the junction temperature:

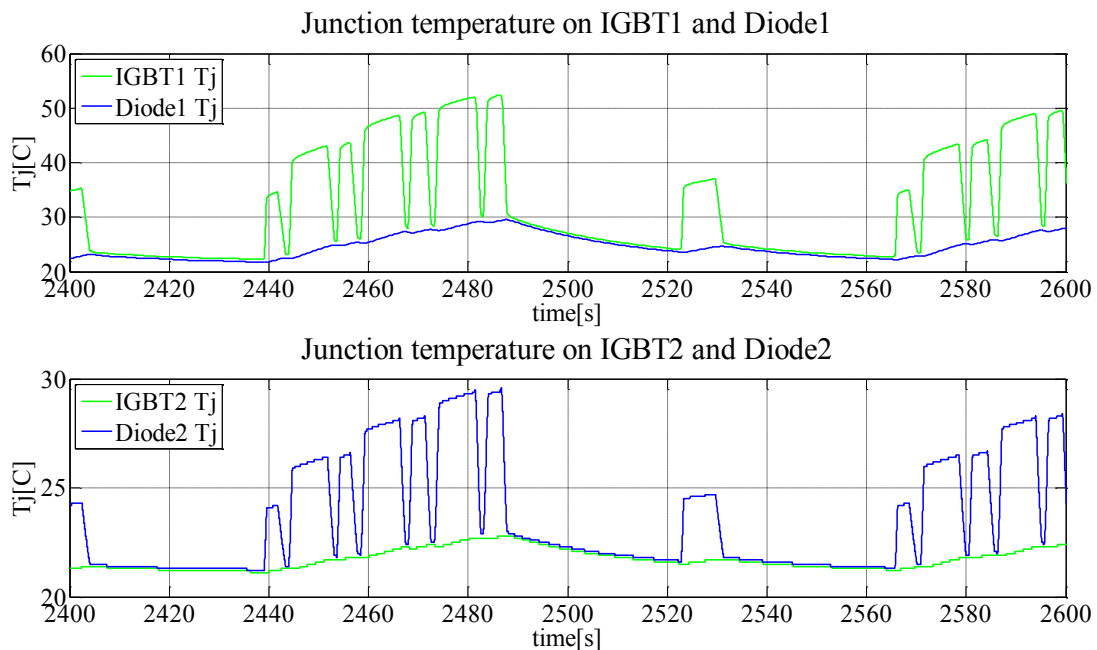


Figure 38 Junction temperature variation on IGBT1, Diode1, IGBT2 and Diode2

The distribution of the mean temperatures and temperature ranges among the counted cycles is more diverse than the previous case as it can be seen in Figure 39 and Figure 40. However, also the temperature ranges are smaller.

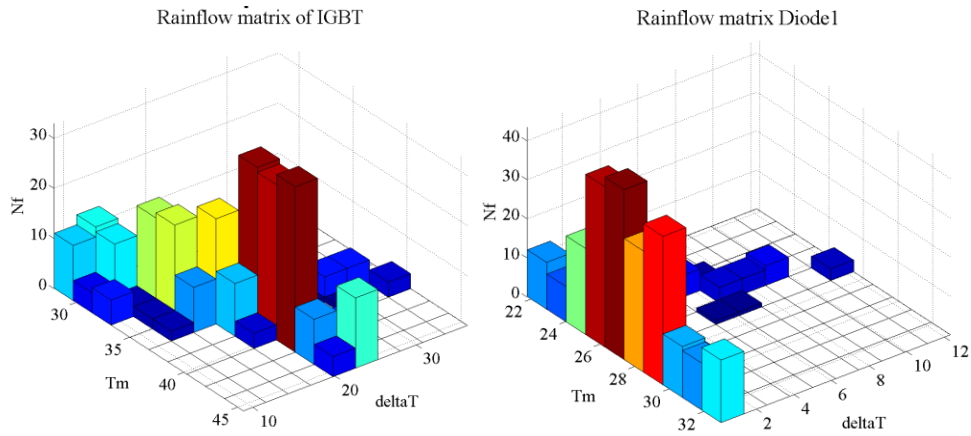


Figure 39 Rainflow 3D matrix for IGBT and Diode1

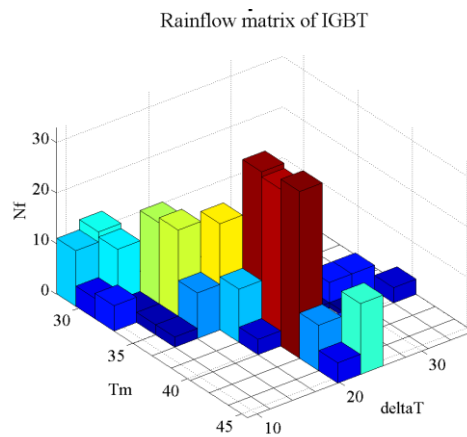


Figure 40 Rainflow 3D matrix for Diode2

The Rainflow histograms are presented as it follows:

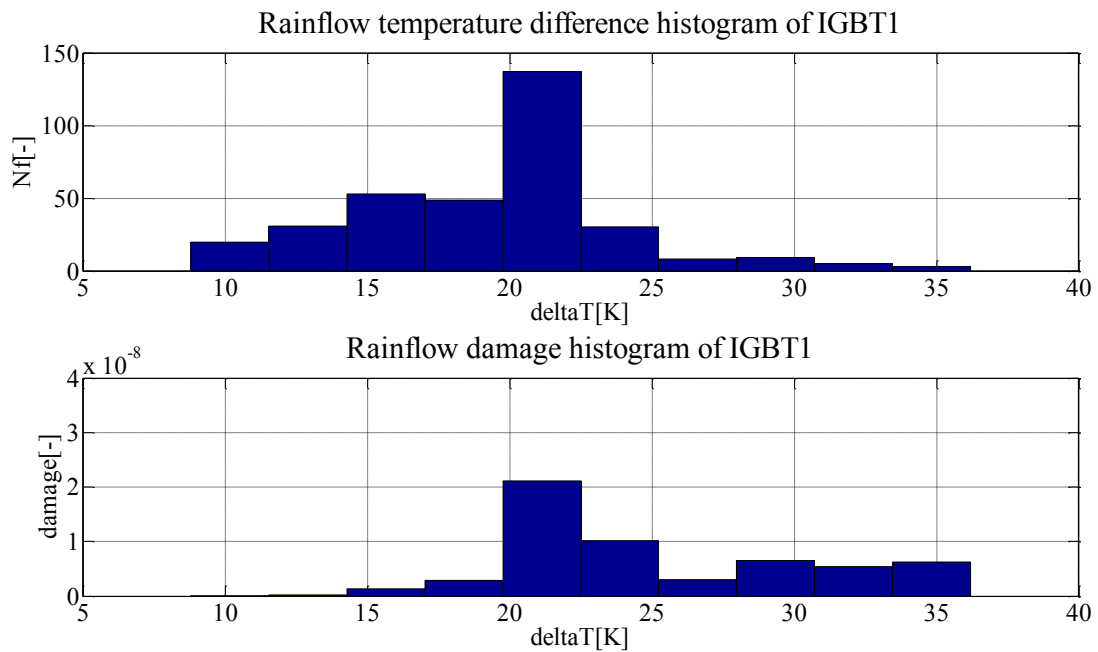


Figure 41 Rainflow and damage histograms on IGBT1

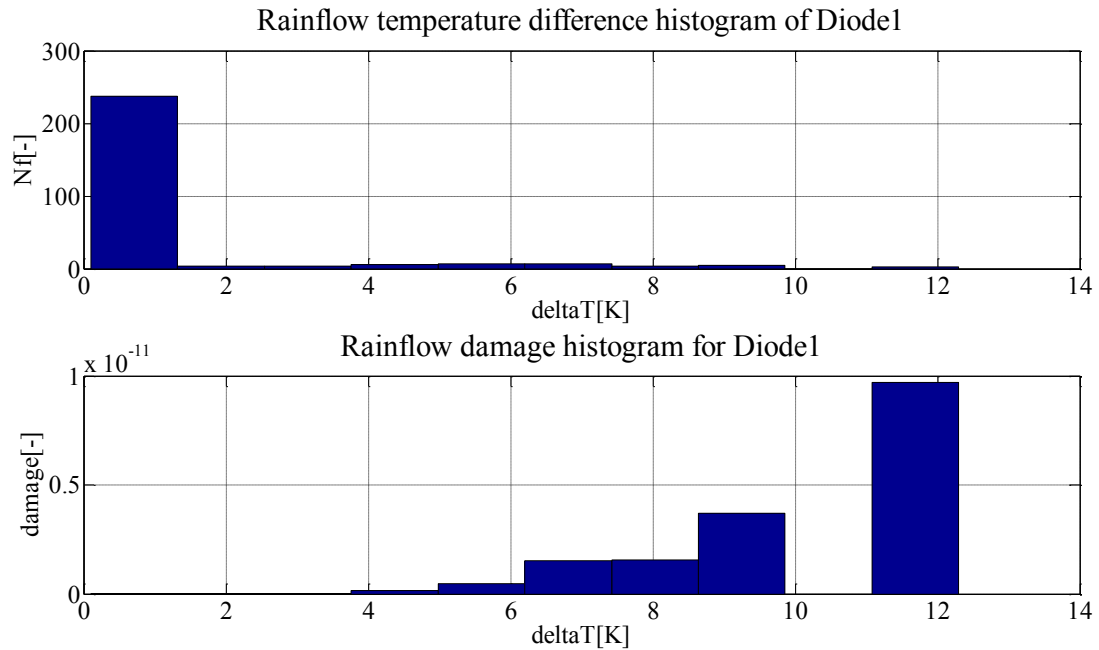


Figure 42 Rainflow and damage histograms on Diode1

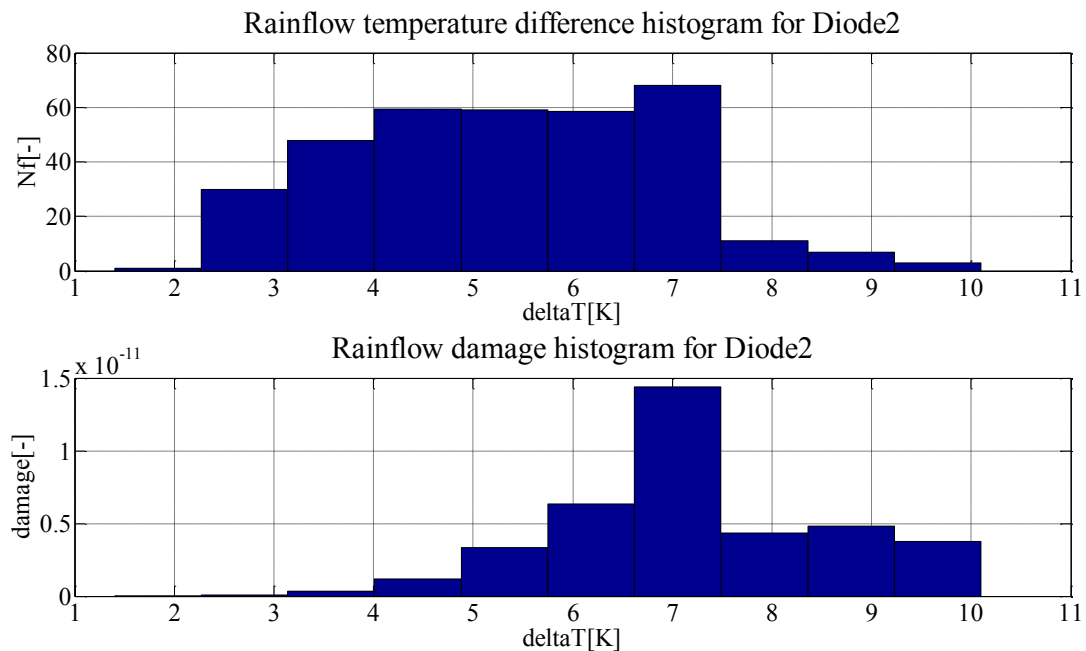


Figure 43 Rainflow and damage histograms of Diode2

As it can be seen from the damage histograms the spikes have a high contribution. After removing them the damage decreases.

The estimated lifetime for the components is: about 7 000 years for IGBT1, 24 mill years for Diode 1 and 11 mill years for Diode 2.

3.6. Simulation with increased water temperature

As presented in the introduction the case where thermal paste gets degraded and as a result the thermal resistance between heatsink and baseplate increases is simulated here by increasing the water temperature at 80°C. As a result the temperature differences increases but not significantly, whereas the mean temperature increases towards 100°C and up to 120°C in the case of the IGBT. These aspects are visible in the Rainflow 3D matrices below:

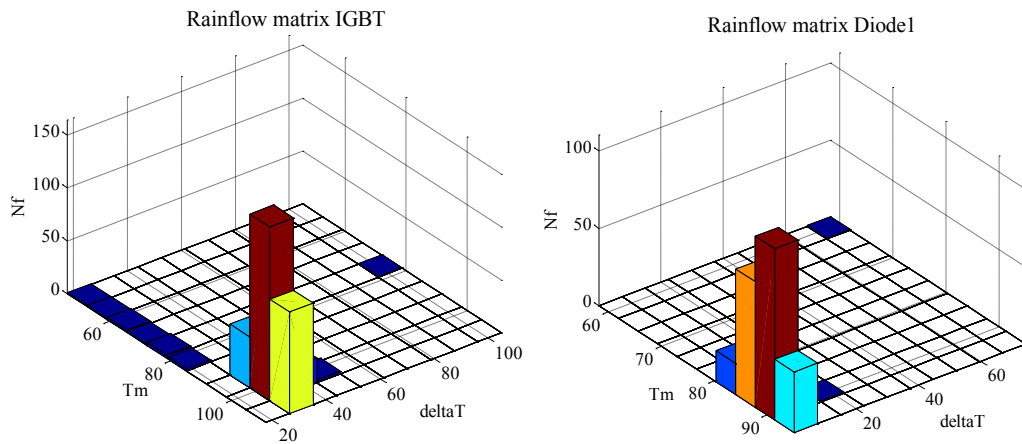


Figure 44 Rainflow 3D matrices for IGBT and Diode 1

Rainflow matrix Diode2

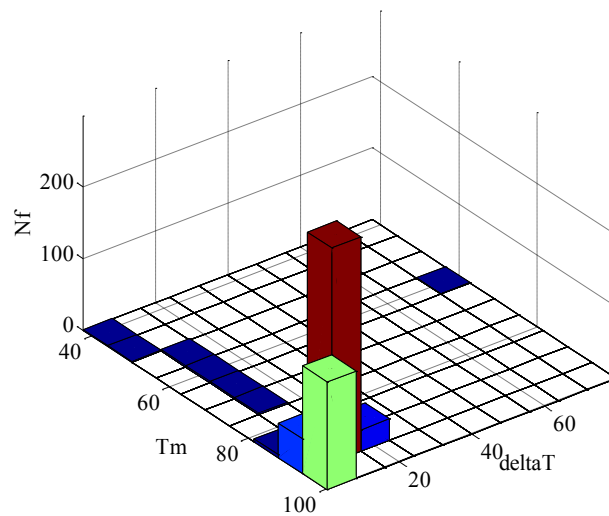


Figure 45 Rainflow 3D matrix for Diode 2

The Rainflow damage histograms of the components are presented in Figure 47, Figure 48 and Figure 49:

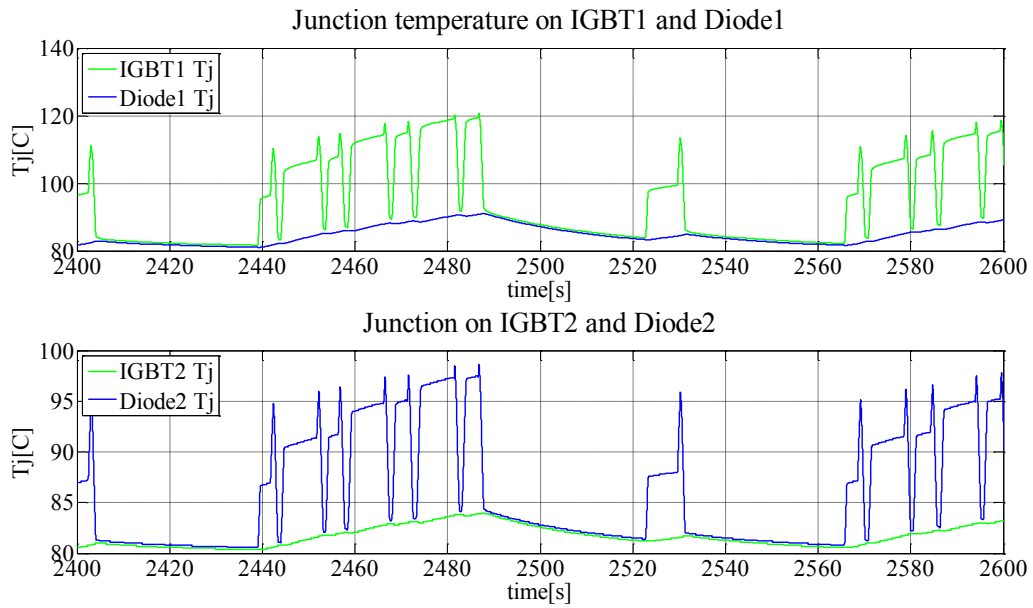


Figure 46 Part of temperature profile when the water temperature gets increased to 80°C

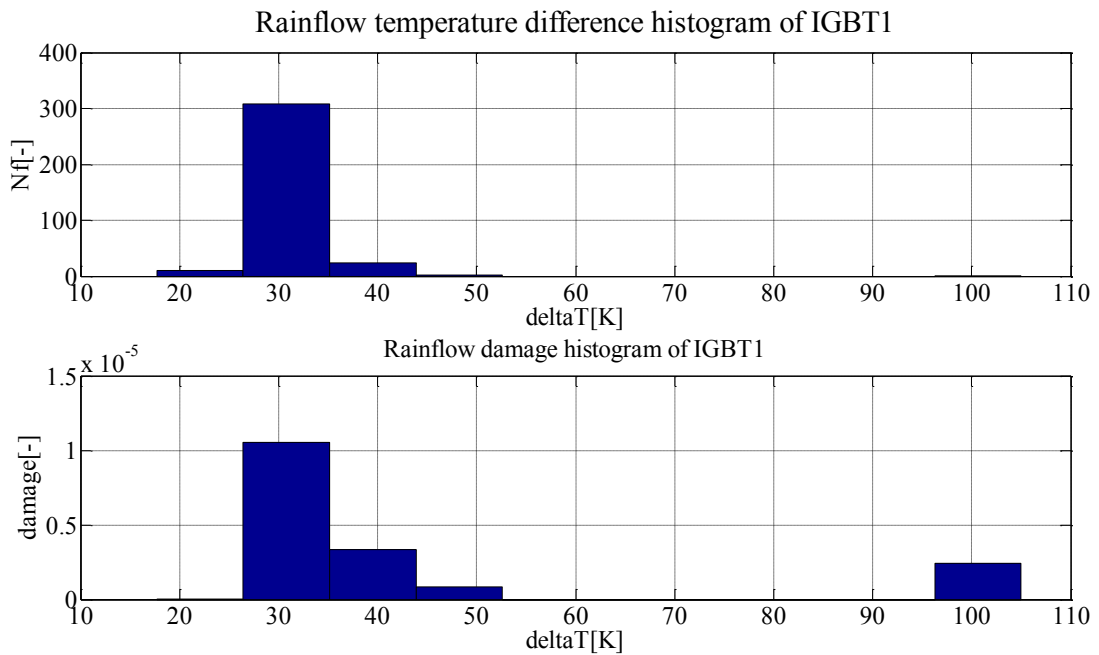


Figure 47 Rainflow histograms of the distribution of ranges of temperature among cycles and the produced damage for IGBT

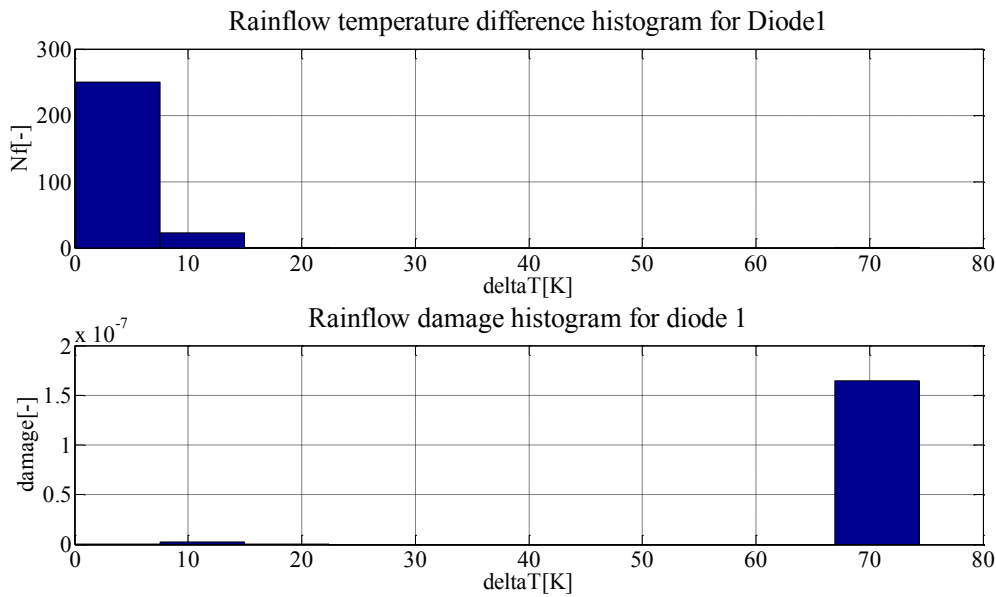


Figure 48 Rainflow histograms of the distribution of ranges of temperature among cycles and the produced damage for Diode1

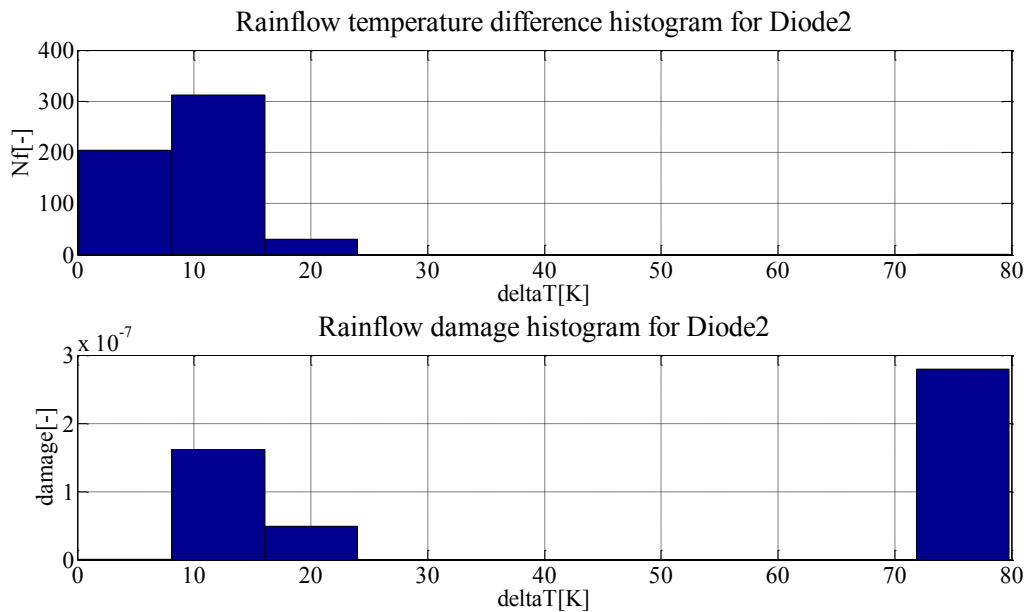


Figure 49 Rainflow histograms of the distribution of ranges of temperature among cycles and the produced damage for Diode2

The lifetime of the IGBT was decreased to about 25 years, 2500 years for Diode 1 and 860 years for Diode 2.

3.7. Summary

An irregular current profile has been fed into the electro-thermal model of the H-bridge. Rainflow cycle counting has been performed on the junction temperature profiles of each component of the module and based on the damage histograms it has been concluded that the most stressed component is the IGBT, followed by Diode 2 and Diode 1.

By removing the spike it has been observed that its influence on the lifetime of the semiconductors is high. The lifetime of the components has been found to be almost double in the case of IGBT1 and almost three times higher for Diode 2.

The temperature of the water was increased up to 80°C and the temperature ranges of the cycles changed, but more significantly the mean temperature.

The results are summarized in Table 4:

Table 4 Summary of simulations results

Water temperature	'Chimney'	IGBT lifetime	Diode 1 lifetime	Diode 2 lifetime
$T_{\text{water}}=21^{\circ}\text{C}$	Present	4000 years	20 mill years	4 mill years
	Removed	7000 years	24 mill years	11 mill years
$T_{\text{water}}=80^{\circ}\text{C}$	Present	25 years	2500 years	860 years

4. Conclusion

An electro-thermal model has been developed and simulated using PLECS toolbox. As a starting point a standard current profile has been fed into the model in order to have an idea about the expected junction temperature on the IGBT and diodes.

Afterwards, the measured current profile has been used for the simulation for three case scenarios:

1. Mission profile fed into the system and the water temperature of the cooling system of 21°C
2. Mission profile with the removed 'chimney' and water temperature of 21°C
3. Mission profile fed into the system with water temperature of 80°C. This simulation was for the case when the thermal grease is degraded and the thermal resistance between heatsink and baseplate is increased. The reason for doing that was to check the validity of the model as a high number of expected years for the lifetime of IGBT and diodes was obtained with the first 2 scenarios.

4.1. Contributions

The model calculates correctly the power losses and the junction temperature can be obtained for the IGBT and diodes.

Rainflow cycle counting can be performed on an irregular temperature profile and by the use of Rainflow 3D matrix it is easy to visualize how the average temperature and temperature ranges are distributed among the counted cycles.

Rainflow damage histogram shows how the temperature differences are affecting the IGBT and diodes by the use of Coffin Manson law and Palmgren Miner rule.

The model still needs to be checked in the future to see how accurate the results are, but for the case of $T_{\text{water}}=21^{\circ}\text{C}$ and with the 'chimney' both mean temperature and temperature swings are low. The part of the mission profiles contains few cycles (approximately 350 for 13404s lengths). After some repetitive cycles of different temperature it follows a time period with no ramps, sometimes even higher than 1000 s (about 16 min) and going up to 3000-4000s the longest (between 50-66 min). During these periods the system is cooled down.

For the simulation without 'chimney' the amplitudes and mean temperatures are much smaller, so the lifetime was expected to increase significantly.

In the case of the simulation with $T_{\text{water}}=80^{\circ}\text{C}$ both the range of temperature and especially the mean temperature are increased. This leads to a significant decrease in the expected lifetime.

4.2. Limitations

Without a further check it is not possible to know how accurate the model is. It behaves as expected, but the obtained lifetimes for the first two scenarios are unrealistic and for the third case it is not possible to confirm it or not.

5. Future work

The model behaves as it should, but it needs to be checked for a 1 year mission profile or based on some obtained experimental data for the case of the power module used.

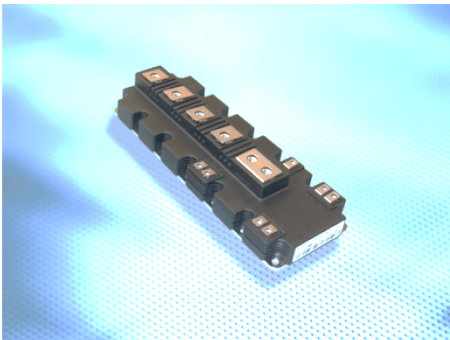
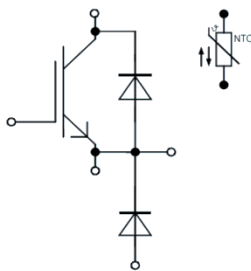
A 3D Rainflow matrix could be implemented in order to have a better view of the picture and know how the combination of mean temperature and temperature ranges damages the devices.

Bibliography

- [1] J. Zed, G. Kalsoom and N. Muhammad, “Accelerated Life Testing of Electronic Components,” in *International Bhurban Conference on Applied Sciences & Technology*, Islamabad, 2011.
- [2] S. Yang, A. Bryant, P. Mawby, D. Xiang, L. Ran and P. Tavner, “An industry-based survey of reliability in power electronic converters,” in *Energy Conversion Congress and Exposition (ECCE)*, San Jose, 2009.
- [3] C. Busca, R. Teodorescu, F. Blaabjerg, S. Munk-Nielsen, L. Helle, T. Abeyasekera and P. Rodriguez, “An overview of the reliability prediction related aspects of high power IGBTs in wind power applications,” in *Proceedings of the 22th European Symposium on the RELIABILITY OF ELECTRON DEVICES, FAILURE PHYSICS AND ANALYSIS*, 2011.
- [4] B. Williams, *Power Electronics: Devices, Drivers, Applications, and and Passive Components*, McGraw-Hill, 1992.
- [5] Infineon, “Technical information datasheet DF1400R12IPAD,” Available at: <http://www.infineon.com/dgdl?folderId=db3a304412b407950112b4095b0601e3&fileId=db3a30431ddc9372011e398afc1a5e4a>.
- [6] C. Busca, “Modeling Lifetime of High Power IGBTs in Wind Power Applications – An overview,” in *Industrial Electronics (ISIE), 2011 IEEE International Symposium*, Gdansk, 2011.
- [7] K. Fischer, T. Stalin, H. Ramberg, T. Thiringer, J. Wenske and R. Karlsson, “Investigation of converter failure in wind turbines,” *Elforsk*, 2012.
- [8] Infineon, “Technical information IGBT modules. Use of Power Cycling curves for IGBT 4,” Available at: <http://www.infineon.com/dgdl/Infineon+-+AN2010-02+-+Use+of+Power+Cycling+Curves+for+IGBT4.pdf?folderId=db3a304412b407950112b4095b0601e3&fileId=db3a30433fa9412f013fc2647c921a4d>.
- [9] C. Bajracharya, M. Molinas, J. Are Suul and T. M. Undeland, “Understanding of tuning techniques of converter controllers for VSC-HVDC,” in *Nordic Workshop on Power and Industrial Electronics*, 2008.
- [10] C. L. Philips and J. M. Parr, *Feedback control systems*, Pearson, 2011.
- [11] PLECS, “User manual,” Available at: www.plexim.com/files/plecsmanual.pdf.

- [12] Infineon, “Thermal equivalent circuit models,” Available at: <http://www.infineon.com/dgdl/Infineon+++AN2008-03+-+Thermal+equivalent+circuit+models.pdf?folderId=db3a304412b407950112b4095b0601e3&fileId=db3a30431a5c32f2011aa65358394dd2>, Application Note AN2008-03, 2008.
- [13] A. Nieslony, “Rainflow Counting Algorithm,” Available at: <http://www.mathworks.com/matlabcentral/fileexchange/3026-rainflow-counting-algorithm>.
- [14] Y.-L. Lee, M. E. Barkey and H.-T. Kang, “Metal Fatigue Analysis Handbook,” Elsevier Inc., 2011.
- [15] *ASTM E1049 - 85(2011)e1 Standard Practices for Cycle Counting in Fatigue Analysis*, 2011.
- [16] J. Due and Ø. R. Nielsen, “Lifetime investigation of high power IGBT modules,” Master thesis, Aalborg University, Aalborg, 2009-2010.
- [17] A. Nieslony, “Determination of fragments of multiaxial service loading strongly influencing the fatigue of machine components,” *Mechanical Systems and Signal Processing*, pp. 2712-2721, 2009.
- [18] R. I. Stephens, A. Fatemi, R. R. Stephens and H. O. Fuchs, *Metal Fatigue in Engineering*, 2nd Edition, Wiley, 2000.
- [19] L. Y.L., M.E.Barkey and H.T.Kang, *Metal Fatigue Analysis Handbook*, Elsevier, 2012.
- [20] P. Tavner, *Reliability & Availability of Wind Turbine Electrical & Electronic Components*, Helsinki: ReliaWind, 2009.

Appendix A

Technische Information / Technical Information															
IGBT-Module IGBT-modules		FD1400R12IP4D													
<p>PrimePACK™3 Modul mit Trench/Feldstopp IGBT4, größerer Emitter Controlled 4 Diode PrimePACK™3 module with Trench/Fieldstop IGBT4, enlarged Emitter Controlled 4 diode</p> <p>Vorläufige Daten / Preliminary Data</p> <div style="display: flex; justify-content: space-around;"> <div style="text-align: center;">  </div> <div style="text-align: center;">  </div> </div> <p>$V_{CES} = 1200V$ $I_{C\ nom} = 1400A / I_{CRM} = 2800A$</p> <div style="display: flex; justify-content: space-between;"> <div style="width: 48%;"> <p>Typische Anwendungen</p> <ul style="list-style-type: none"> • Chopper-Anwendungen <p>Elektrische Eigenschaften</p> <ul style="list-style-type: none"> • Erweiterte Sperrschichttemperatur $T_{vj\ op}$ • Große DC-Festigkeit • Hohe Kurzschlussrobustheit, selbstlimitierender Kurzschlussstrom • V_{CEsat} mit positivem Temperaturkoeffizienten • Niedriges V_{CEsat} <p>Mechanische Eigenschaften</p> <ul style="list-style-type: none"> • 4 kV AC 1min Isolationsfestigkeit • Gehäuse mit CTI > 400 • Große Luft- und Kriechstrecken • Hohe Last- und thermische Wechselfestigkeit • Hohe Leistungsdichte • Substrat für kleinen thermischen Widerstand </div> <div style="width: 48%;"> <p>Typical Applications</p> <ul style="list-style-type: none"> • Chopper Applications <p>Electrical Features</p> <ul style="list-style-type: none"> • Extended Operation Temperature $T_{vj\ op}$ • High DC Stability • High Short Circuit Capability, Self Limiting Short Circuit Current • V_{CEsat} with positive Temperature Coefficient • Low V_{CEsat} <p>Mechanical Features</p> <ul style="list-style-type: none"> • 4 kV AC 1min Insulation • Package with CTI > 400 • High Creepage and Clearance Distances • High Power and Thermal Cycling Capability • High Power Density • Substrate for Low Thermal Resistance </div> </div>															
Module Label Code															
Barcode Code 128		Content of the Code													
		<table border="1"> <thead> <tr> <th>Content of the Code</th> <th>Digit</th> </tr> </thead> <tbody> <tr> <td>Module Serial Number</td> <td>1 - 5</td> </tr> <tr> <td>Module Material Number</td> <td>6 - 11</td> </tr> <tr> <td>Production Order Number</td> <td>12 - 19</td> </tr> <tr> <td>Datecode (Production Year)</td> <td>20 - 21</td> </tr> <tr> <td>Datecode (Production Week)</td> <td>22 - 23</td> </tr> </tbody> </table>		Content of the Code	Digit	Module Serial Number	1 - 5	Module Material Number	6 - 11	Production Order Number	12 - 19	Datecode (Production Year)	20 - 21	Datecode (Production Week)	22 - 23
Content of the Code	Digit														
Module Serial Number	1 - 5														
Module Material Number	6 - 11														
Production Order Number	12 - 19														
Datecode (Production Year)	20 - 21														
Datecode (Production Week)	22 - 23														
DMX - Code															
															
prepared by: AC	date of publication: 2013-03-06														
approved by: MS	revision: 2.3	UL approved (E83335)													

Technische Information / Technical Information					
IGBT-Module IGBT-modules					FD1400R12IP4D
Vorläufige Daten Preliminary Data					
IGBT-Chopper / IGBT-Chopper Höchstzulässige Werte / Maximum Rated Values					
Kollektor-Emitter-Sperrspannung Collector-emitter voltage	$T_{vj} = 25^{\circ}\text{C}$	V_{CES}	1200	V	
Kollektor-Dauergleichstrom Continuous DC collector current	$T_C = 100^{\circ}\text{C}, T_{vj} = 175^{\circ}\text{C}$	$I_{C\text{ nom}}$	1400	A	
Periodischer Kollektor-Spitzenstrom Repetitive peak collector current	$t_p = 1\text{ ms}$	I_{CRM}	2800	A	
Gesamt-Verlustleistung Total power dissipation	$T_C = 25^{\circ}\text{C}, T_{vj} = 175^{\circ}\text{C}$	P_{tot}	7,70	kW	
Gate-Emitter-Spitzenspannung Gate-emitter peak voltage		V_{GES}	+/-20	V	
Charakteristische Werte / Characteristic Values					
			min.	typ.	max.
Kollektor-Emitter-Sättigungsspannung Collector-emitter saturation voltage	$I_C = 1400\text{ A}, V_{GE} = 15\text{ V}$ $I_C = 1400\text{ A}, V_{GE} = 15\text{ V}$ $I_C = 1400\text{ A}, V_{GE} = 15\text{ V}$	$T_{vj} = 25^{\circ}\text{C}$ $T_{vj} = 125^{\circ}\text{C}$ $T_{vj} = 150^{\circ}\text{C}$	$V_{CE\text{ sat}}$	1,75 2,05 2,15	2,10 V V V
Gate-Schwellenspannung Gate threshold voltage	$I_C = 49,0\text{ mA}, V_{CE} = V_{GE}, T_{vj} = 25^{\circ}\text{C}$		V_{Geth}	5,0	5,8 6,5
Gateladung Gate charge	$V_{GE} = -15\text{ V} \dots +15\text{ V}$		Q_G	9,60	μC
Interner Gatewiderstand Internal gate resistor	$T_{vj} = 25^{\circ}\text{C}$		R_{Gint}	0,8	Ω
Eingangskapazität Input capacitance	$f = 1\text{ MHz}, T_{vj} = 25^{\circ}\text{C}, V_{CE} = 25\text{ V}, V_{GE} = 0\text{ V}$		C_{ies}	82,0	nF
Rückwirkungskapazität Reverse transfer capacitance	$f = 1\text{ MHz}, T_{vj} = 25^{\circ}\text{C}, V_{CE} = 25\text{ V}, V_{GE} = 0\text{ V}$		C_{res}	4,60	nF
Kollektor-Emitter-Reststrom Collector-emitter cut-off current	$V_{CE} = 1200\text{ V}, V_{GE} = 0\text{ V}, T_{vj} = 25^{\circ}\text{C}$		I_{CES}		5,0 mA
Gate-Emitter-Reststrom Gate-emitter leakage current	$V_{CE} = 0\text{ V}, V_{GE} = 20\text{ V}, T_{vj} = 25^{\circ}\text{C}$		I_{GES}		400 nA
Einschaltverzögerungszeit, induktive Last Turn-on delay time, inductive load	$I_C = 1400\text{ A}, V_{CE} = 600\text{ V}$ $V_{GE} = \pm 15\text{ V}$ $R_{Gon} = 1,0\ \Omega$	$T_{vj} = 25^{\circ}\text{C}$ $T_{vj} = 125^{\circ}\text{C}$ $T_{vj} = 150^{\circ}\text{C}$	$t_{d\text{ on}}$	0,20 0,21 0,21	μs μs μs
Anstiegszeit, induktive Last Rise time, inductive load	$I_C = 1400\text{ A}, V_{CE} = 600\text{ V}$ $V_{GE} = \pm 15\text{ V}$ $R_{Gon} = 1,0\ \Omega$	$T_{vj} = 25^{\circ}\text{C}$ $T_{vj} = 125^{\circ}\text{C}$ $T_{vj} = 150^{\circ}\text{C}$	t_r	0,12 0,13 0,13	μs μs μs
Abschaltverzögerungszeit, induktive Last Turn-off delay time, inductive load	$I_C = 1400\text{ A}, V_{CE} = 600\text{ V}$ $V_{GE} = \pm 15\text{ V}$ $R_{Goff} = 1,0\ \Omega$	$T_{vj} = 25^{\circ}\text{C}$ $T_{vj} = 125^{\circ}\text{C}$ $T_{vj} = 150^{\circ}\text{C}$	$t_{d\text{ off}}$	0,87 0,95 0,97	μs μs μs
Fallzeit, induktive Last Fall time, inductive load	$I_C = 1400\text{ A}, V_{CE} = 600\text{ V}$ $V_{GE} = \pm 15\text{ V}$ $R_{Goff} = 1,0\ \Omega$	$T_{vj} = 25^{\circ}\text{C}$ $T_{vj} = 125^{\circ}\text{C}$ $T_{vj} = 150^{\circ}\text{C}$	t_f	0,20 0,23 0,23	μs μs μs
Einschaltverlustenergie pro Puls Turn-on energy loss per pulse	$I_C = 1400\text{ A}, V_{CE} = 600\text{ V}, L_S = 30\text{ nH}$ $V_{GE} = \pm 15\text{ V}, di/dt = 8600\text{ A}/\mu\text{s} (T_{vj}=150^{\circ}\text{C})$ $R_{Gon} = 1,0\ \Omega$	$T_{vj} = 25^{\circ}\text{C}$ $T_{vj} = 125^{\circ}\text{C}$ $T_{vj} = 150^{\circ}\text{C}$	E_{on}	65,0 80,0 95,0	mJ mJ mJ
Abschaltverlustenergie pro Puls Turn-off energy loss per pulse	$I_C = 1400\text{ A}, V_{CE} = 600\text{ V}, L_S = 30\text{ nH}$ $V_{GE} = \pm 15\text{ V}, du/dt = 2700\text{ V}/\mu\text{s} (T_{vj}=150^{\circ}\text{C})$ $R_{Goff} = 1,0\ \Omega$	$T_{vj} = 25^{\circ}\text{C}$ $T_{vj} = 125^{\circ}\text{C}$ $T_{vj} = 150^{\circ}\text{C}$	E_{off}	180 250 280	mJ mJ mJ
Kurzschlußverhalten SC data	$V_{GE} \leq 15\text{ V}, V_{CC} = 800\text{ V}$ $V_{CE\text{ max}} = V_{CES} - L_{SCE} \cdot di/dt$	$t_p \leq 10\ \mu\text{s}, T_{vj} = 150^{\circ}\text{C}$	I_{SC}	5600	A
Wärmewiderstand, Chip bis Gehäuse Thermal resistance, junction to case	pro IGBT / per IGBT		R_{thJC}		19,5 K/kW
Wärmewiderstand, Gehäuse bis Kühlkörper Thermal resistance, case to heatsink	pro IGBT / per IGBT $\lambda_{paste} = 1\text{ W}/(\text{m}\cdot\text{K}) / \lambda_{grease} = 1\text{ W}/(\text{m}\cdot\text{K})$		R_{thCH}	9,30	K/kW
prepared by: AC	date of publication: 2013-03-06				
approved by: MS	revision: 2.3				

Technische Information / Technical Information					
IGBT-Module IGBT-modules					
FD1400R12IP4D		Vorläufige Daten Preliminary Data			
Diode-Chopper / Diode-Chopper					
Höchstzulässige Werte / Maximum Rated Values					
Periodische Spitzenspernung Repetitive peak reverse voltage	$T_{vj} = 25^{\circ}\text{C}$	V_{RRM}	1200	V	
Dauergleichstrom Continuous DC forward current		I_F	1400	A	
Periodischer Spitzenstrom Repetitive peak forward current	$t_p = 1\text{ ms}$	I_{FRM}	2800	A	
Grenzlastintegral I^2t - value	$V_R = 0\text{ V}, t_p = 10\text{ ms}, T_{vj} = 125^{\circ}\text{C}$ $V_R = 0\text{ V}, t_p = 10\text{ ms}, T_{vj} = 150^{\circ}\text{C}$	I^2t	270 260	kA^2s kA^2s	
Charakteristische Werte / Characteristic Values					
			min.	typ.	max.
Durchlassspannung Forward voltage	$I_F = 1400\text{ A}, V_{GE} = 0\text{ V}$ $I_F = 1400\text{ A}, V_{GE} = 0\text{ V}$ $I_F = 1400\text{ A}, V_{GE} = 0\text{ V}$	$T_{vj} = 25^{\circ}\text{C}$ $T_{vj} = 125^{\circ}\text{C}$ $T_{vj} = 150^{\circ}\text{C}$	V_F	1,65 1,55 1,55	2,15 V V
Rückstromspitze Peak reverse recovery current	$I_F = 1400\text{ A}, -di_F/dt = 8600\text{ A}/\mu\text{s} (T_{vj}=150^{\circ}\text{C})$ $V_R = 600\text{ V}$	$T_{vj} = 25^{\circ}\text{C}$ $T_{vj} = 125^{\circ}\text{C}$ $T_{vj} = 150^{\circ}\text{C}$	I_{RM}	1000 1200 1250	A A A
Sperrverzögerungsladung Recovered charge	$I_F = 1400\text{ A}, -di_F/dt = 8600\text{ A}/\mu\text{s} (T_{vj}=150^{\circ}\text{C})$ $V_R = 600\text{ V}$	$T_{vj} = 25^{\circ}\text{C}$ $T_{vj} = 125^{\circ}\text{C}$ $T_{vj} = 150^{\circ}\text{C}$	Q_r	170 300 330	μC μC μC
Abschaltenergie pro Puls Reverse recovery energy	$I_F = 1400\text{ A}, -di_F/dt = 8600\text{ A}/\mu\text{s} (T_{vj}=150^{\circ}\text{C})$ $V_R = 600\text{ V}$	$T_{vj} = 25^{\circ}\text{C}$ $T_{vj} = 125^{\circ}\text{C}$ $T_{vj} = 150^{\circ}\text{C}$	E_{rec}	80,0 140 160	mJ mJ mJ
Wärmewiderstand, Chip bis Gehäuse Thermal resistance, junction to case	pro Diode / per diode	$R_{th(jc)}$		25,0	K/kW
Wärmewiderstand, Gehäuse bis Kühlkörper Thermal resistance, case to heatsink	pro Diode / per diode $\lambda_{paste} = 1\text{ W}/(\text{m}\cdot\text{K}) / \lambda_{grbase} = 1\text{ W}/(\text{m}\cdot\text{K})$	$R_{th(ch)}$	17,0		K/kW
Diode, Revers / Diode, Reverse					
Höchstzulässige Werte / Maximum Rated Values					
Periodische Spitzenspernung Repetitive peak reverse voltage	$T_{vj} = 25^{\circ}\text{C}$	V_{RRM}	1200	V	
Dauergleichstrom Continuous DC forward current		I_F	180	A	
Periodischer Spitzenstrom Repetitive peak forward current	$t_p = 1\text{ ms}$	I_{FRM}	360	A	
Grenzlastintegral I^2t - value	$V_R = 0\text{ V}, t_p = 10\text{ ms}, T_{vj} = 125^{\circ}\text{C}$	I^2t	0,23	kA^2s	
Charakteristische Werte / Characteristic Values					
			min.	typ.	max.
Durchlassspannung Forward voltage	$I_F = 180\text{ A}, V_{GE} = 0\text{ V}$ $I_F = 180\text{ A}, V_{GE} = 0\text{ V}$	$T_{vj} = 25^{\circ}\text{C}$ $T_{vj} = 125^{\circ}\text{C}$	V_F	1,65 1,65	2,15 V V
Wärmewiderstand, Chip bis Gehäuse Thermal resistance, junction to case	pro Diode / per diode	$R_{th(jc)}$		225	K/kW
Wärmewiderstand, Gehäuse bis Kühlkörper Thermal resistance, case to heatsink	pro Diode / per diode $\lambda_{paste} = 1\text{ W}/(\text{m}\cdot\text{K}) / \lambda_{grbase} = 1\text{ W}/(\text{m}\cdot\text{K})$	$R_{th(ch)}$	120		K/kW
prepared by: AC	date of publication: 2013-03-06				
approved by: MS	revision: 2.3				

Technische Information / Technical Information					
IGBT-Module IGBT-modules		FD1400R12IP4D			
		Vorläufige Daten Preliminary Data			
NTC-Widerstand / NTC-Thermistor					
Charakteristische Werte / Characteristic Values					
		min. typ. max.			
Nennwiderstand Rated resistance	$T_C = 25^\circ\text{C}$	R_{25}		5,00	k Ω
Abweichung von R100 Deviation of R100	$T_C = 100^\circ\text{C}, R_{100} = 493 \Omega$	$\Delta R/R$	-5	5	%
Verlustleistung Power dissipation	$T_C = 25^\circ\text{C}$	P_{25}		20,0	mW
B-Wert B-value	$R_2 = R_{25} \exp [B_{25/50}(1/T_2 - 1/(298,15 \text{ K}))]$	$B_{25/50}$		3375	K
B-Wert B-value	$R_2 = R_{25} \exp [B_{25/60}(1/T_2 - 1/(298,15 \text{ K}))]$	$B_{25/60}$		3411	K
B-Wert B-value	$R_2 = R_{25} \exp [B_{25/100}(1/T_2 - 1/(298,15 \text{ K}))]$	$B_{25/100}$		3433	K
Angaben gemäß gültiger Application Note. Specification according to the valid application note.					
Modul / Module					
Isolations-Prüfspannung Isolation test voltage	RMS, f = 50 Hz, t = 1 min.	V_{ISOL}		4,0	kV
Material Modulgrundplatte Material of module baseplate				Cu	
Innere Isolation Internal isolation	Basisisolation (Schutzklasse 1, EN61140) basic insulation (class 1, IEC 61140)			Al_2O_3	
Kriechstreck Creepage distance	Kontakt - Kühlkörper / terminal to heatsink Kontakt - Kontakt / terminal to terminal			33,0 33,0	mm
Luftstrecke Clearance	Kontakt - Kühlkörper / terminal to heatsink Kontakt - Kontakt / terminal to terminal			19,0 19,0	mm
Vergleichszahl der Kriechwegbildung Comperative tracking index		CTI		> 400	
		min. typ. max.			
Modulstreuintuktivität Stray inductance module		L_{SCE}		10	nH
Modulleitungswiderstand, Anschlüsse - Chip Module lead resistance, terminals - chip	$T_C = 25^\circ\text{C}$, pro Schalter / per switch	$R_{\text{CC+EE}}$		0,20	m Ω
Höchstzulässige Sperrschichttemperatur Maximum junction temperature	Wechselrichter, Brems-Chopper / inverter, brake-chopper	$T_{\text{vj max}}$		175	$^\circ\text{C}$
Temperatur im Schaltbetrieb Temperature under switching conditions	Wechselrichter, Brems-Chopper / inverter, brake-chopper	$T_{\text{vj op}}$	-40	150	$^\circ\text{C}$
Lagertemperatur Storage temperature		T_{stg}	-40	150	$^\circ\text{C}$
Anzugsdrehmoment f. Modulmontage Mounting torque for modul mounting	Schraube M5 - Montage gem. gültiger Applikationsschrift Screw M5 - Mounting according to valid application note	M	3,00	-	6,00 Nm
Anzugsdrehmoment f. elektr. Anschlüsse Terminal connection torque	Schraube M8 - Montage gem. gültiger Applikationsschrift Screw M8 - Mounting according to valid application note	M	1,8 8,0	-	2,1 10 Nm
Gewicht Weight		G		1200	g
prepared by: AC		date of publication: 2013-03-06			
approved by: MS		revision: 2.3			

Technische Information / Technical Information

IGBT-Module
IGBT-modules

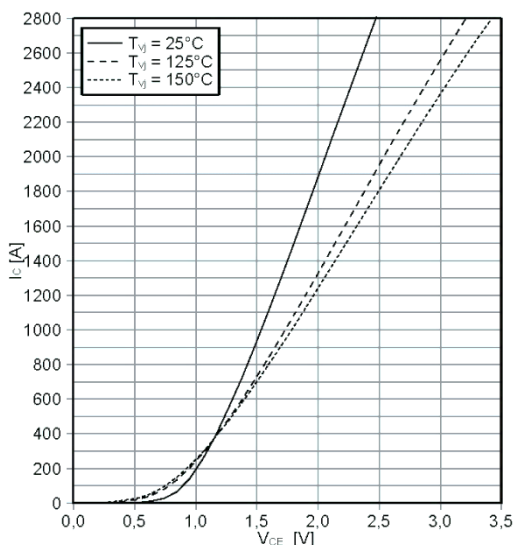
FD1400R12IP4D



Vorläufige Daten
Preliminary Data

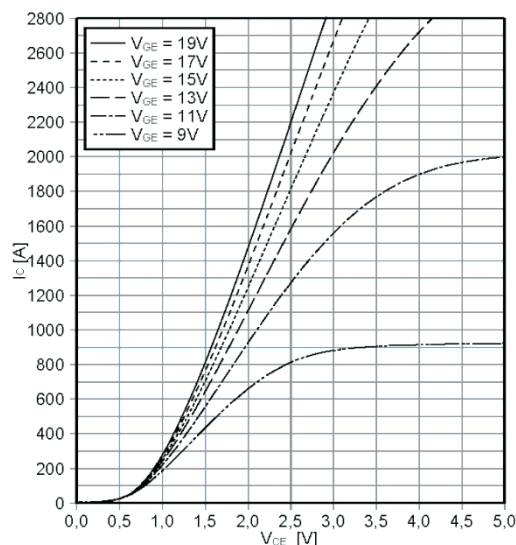
Ausgangskennlinie IGBT-Chopper (typisch)
output characteristic IGBT-Chopper (typical)

$I_C = f(V_{CE})$
 $V_{GE} = 15\text{ V}$



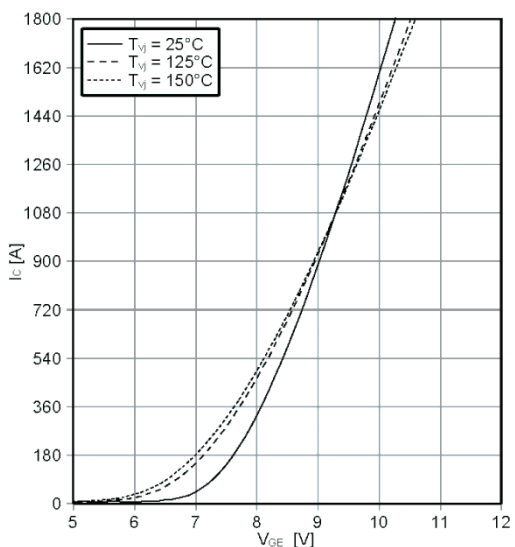
Ausgangskennlinienfeld IGBT-Chopper (typisch)
output characteristic IGBT-Chopper (typical)

$I_C = f(V_{CE})$
 $T_{vj} = 150^\circ\text{C}$



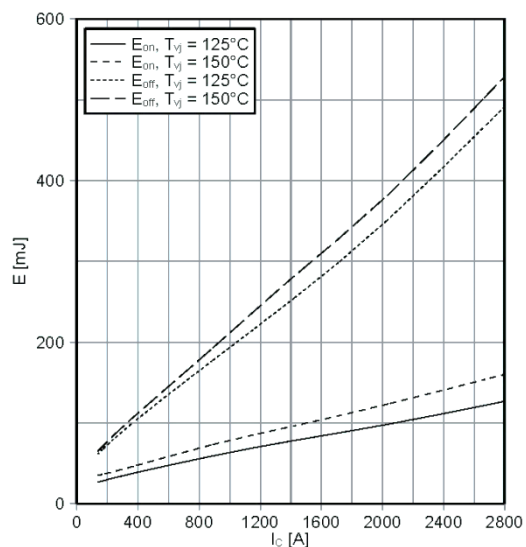
Übertragungscharakteristik IGBT-Chopper (typisch)
transfer characteristic IGBT-Chopper (typical)

$I_C = f(V_{GE})$
 $V_{CE} = 20\text{ V}$



Schaltverluste IGBT-Chopper (typisch)
switching losses IGBT-Chopper (typical)

$E_{on} = f(I_C)$, $E_{off} = f(I_C)$
 $V_{GE} = \pm 15\text{ V}$, $R_{Gon} = 1\ \Omega$, $R_{Goff} = 1\ \Omega$, $V_{CE} = 600\text{ V}$



prepared by: AC	date of publication: 2013-03-06
approved by: MS	revision: 2.3

Technische Information / Technical Information

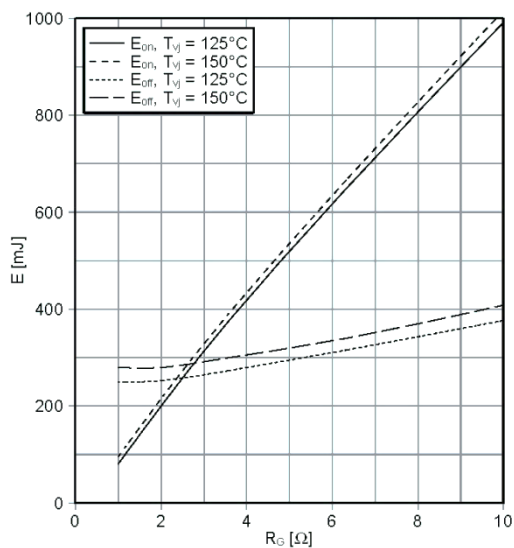
IGBT-Module
IGBT-modules

FD1400R12IP4D

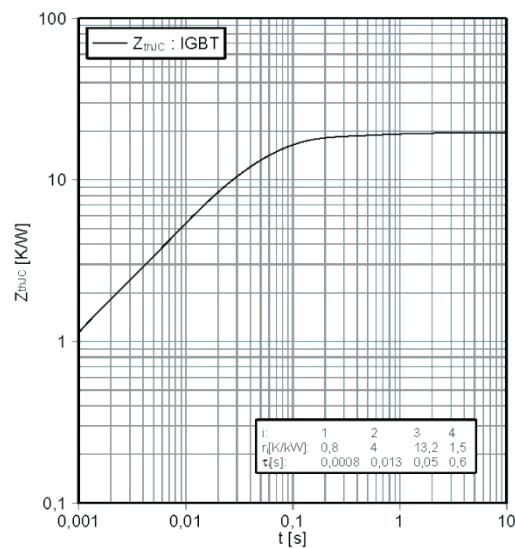


Vorläufige Daten
Preliminary Data

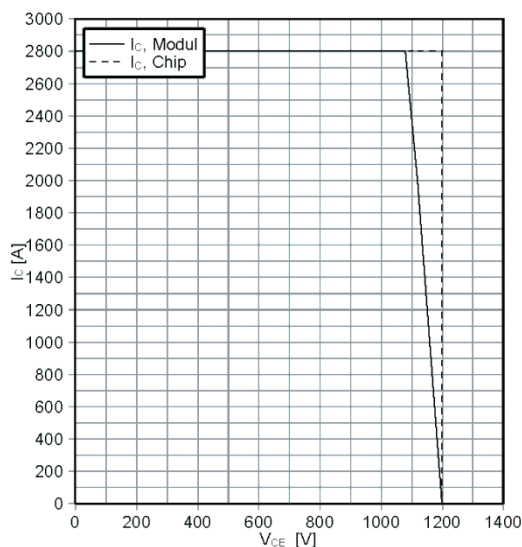
Schaltverluste IGBT-Chopper (typisch)
switching losses IGBT-Chopper (typical)
 $E_{on} = f(R_G)$, $E_{off} = f(R_G)$
 $V_{GE} = \pm 15\text{ V}$, $I_C = 1400\text{ A}$, $V_{CE} = 600\text{ V}$



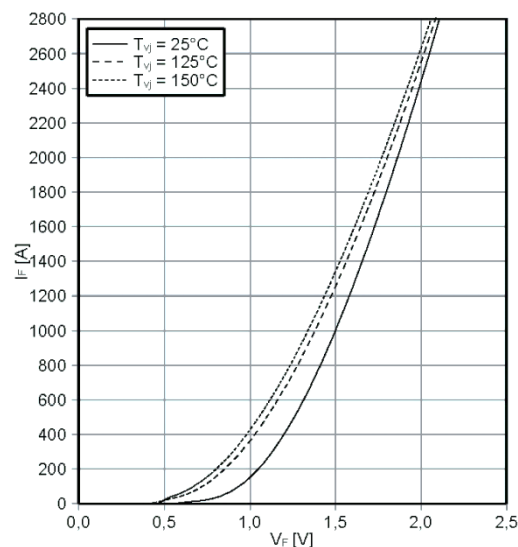
Transienter Wärmewiderstand IGBT-Chopper
transient thermal impedance IGBT-Chopper
 $Z_{thJC} = f(t)$



Sicherer Rückwärts-Arbeitsbereich IGBT-Chopper (RBSOA)
reverse bias safe operating area IGBT-Chopper (RBSOA)
 $I_C = f(V_{CE})$
 $V_{GE} = \pm 15\text{ V}$, $R_{Goff} = 1\ \Omega$, $T_{vj} = 150^\circ\text{C}$



Durchlasskennlinie der Diode-Chopper (typisch)
forward characteristic of Diode-Chopper (typical)
 $I_F = f(V_F)$



prepared by: AC	date of publication: 2013-03-06
approved by: MS	revision: 2.3

Technische Information / Technical Information

IGBT-Module
IGBT-modules

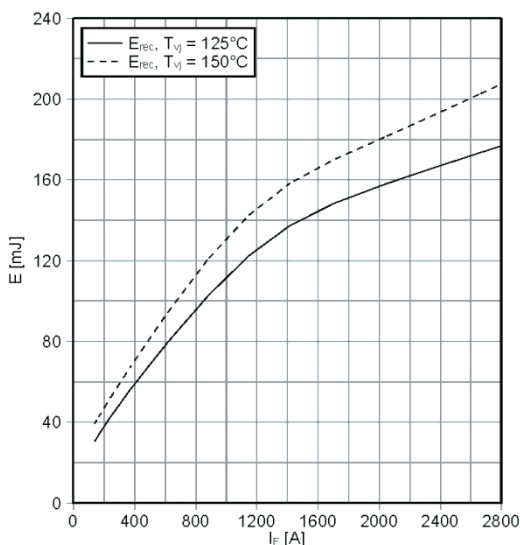
FD1400R12IP4D



Vorläufige Daten
Preliminary Data

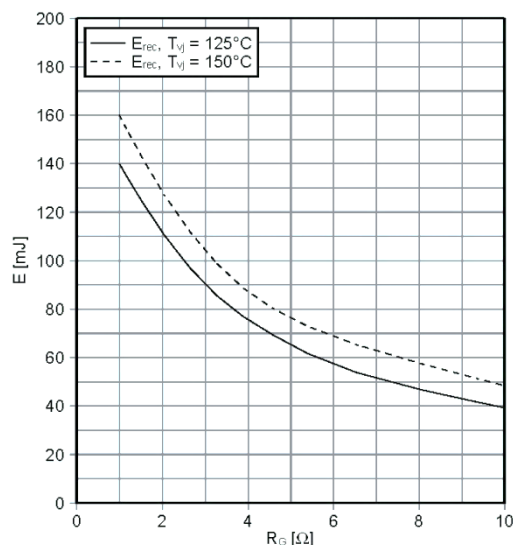
Schaltverluste Diode-Chopper (typisch)
switching losses Diode-Chopper (typical)

$E_{rec} = f(I_F)$
 $R_{Gon} = 1 \Omega, V_{CE} = 600 V$



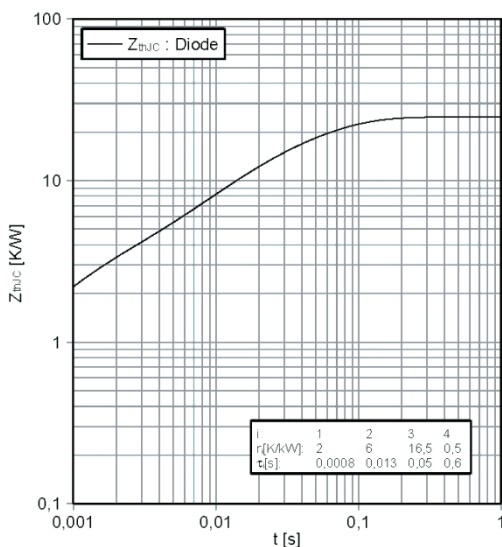
Schaltverluste Diode-Chopper (typisch)
switching losses Diode-Chopper (typical)

$E_{rec} = f(R_G)$
 $I_F = 1400 A, V_{CE} = 600 V$



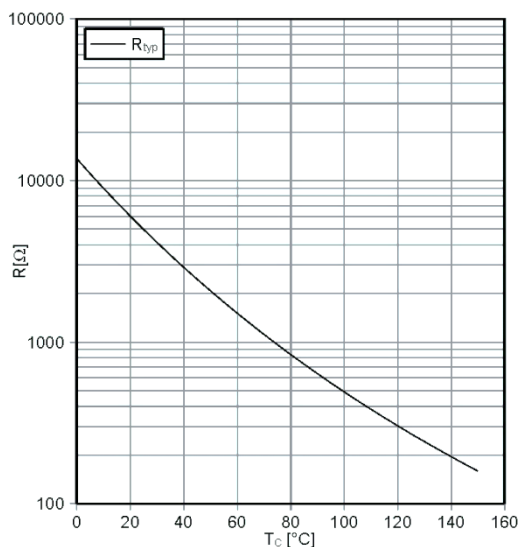
Transienter Wärmewiderstand Diode-Chopper
transient thermal impedance Diode-Chopper

$Z_{thJC} = f(t)$



NTC-Widerstand-Temperaturkennlinie (typisch)
NTC-Thermistor-temperature characteristic (typical)

$R = f(T)$



prepared by: AC	date of publication: 2013-03-06
approved by: MS	revision: 2.3

Technische Information / Technical Information

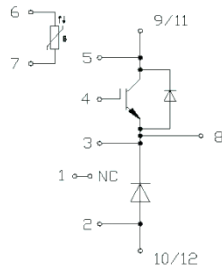
IGBT-Module
IGBT-modules

FD1400R12IP4D

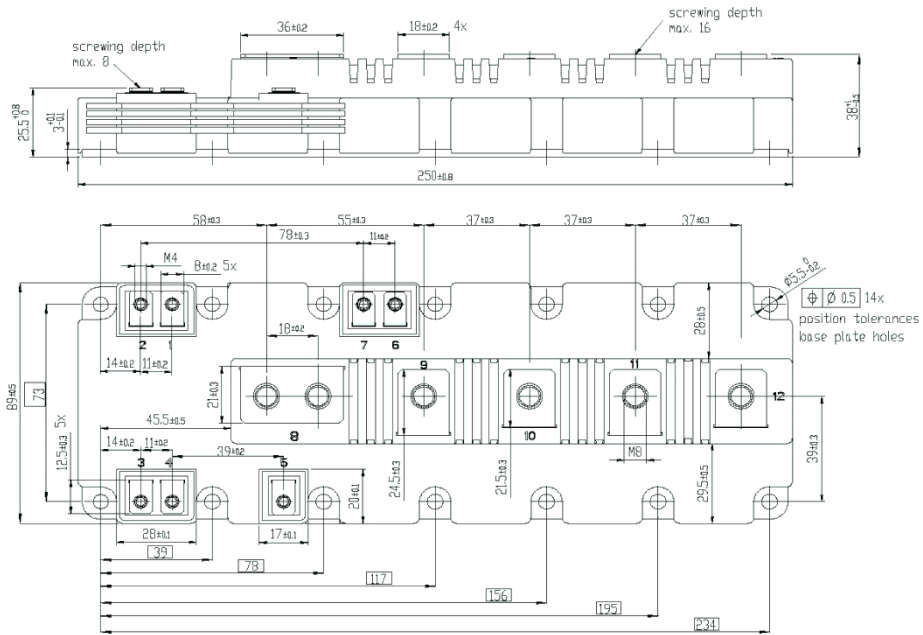


Vorläufige Daten
Preliminary Data

Schaltplan / circuit_diagram_headline



Gehäuseabmessungen / package outlines



prepared by: AC	date of publication: 2013-03-06
approved by: MS	revision: 2.3

Technische Information / Technical Information IGBT-Module IGBT-modules <div style="text-align: center;">FD1400R12IP4D</div>	
Vorläufige Daten Preliminary Data	
Nutzungsbedingungen	
<p>Die in diesem Produktdatenblatt enthaltenen Daten sind ausschließlich für technisch geschultes Fachpersonal bestimmt. Die Beurteilung der Eignung dieses Produktes für Ihre Anwendung sowie die Beurteilung der Vollständigkeit der bereitgestellten Produktdaten für diese Anwendung obliegt Ihnen bzw. Ihren technischen Abteilungen.</p>	
<p>In diesem Produktdatenblatt werden diejenigen Merkmale beschrieben, für die wir eine liefervertragliche Gewährleistung übernehmen. Eine solche Gewährleistung richtet sich ausschließlich nach Maßgabe der im jeweiligen Liefervertrag enthaltenen Bestimmungen. Garantien jeglicher Art werden für das Produkt und dessen Eigenschaften keinesfalls übernommen. Die Angaben in den gültigen Anwendungs- und Montagehinweisen des Moduls sind zu beachten.</p>	
<p>Sollten Sie von uns Produktinformationen benötigen, die über den Inhalt dieses Produktdatenblatts hinausgehen und insbesondere eine spezifische Verwendung und den Einsatz dieses Produktes betreffen, setzen Sie sich bitte mit dem für Sie zuständigen Vertriebsbüro in Verbindung (siehe www.infineon.com, Vertrieb&Kontakt). Für Interessenten halten wir Application Notes bereit.</p>	
<p>Aufgrund der technischen Anforderungen könnte unser Produkt gesundheitsgefährdende Substanzen enthalten. Bei Rückfragen zu den in diesem Produkt jeweils enthaltenen Substanzen setzen Sie sich bitte ebenfalls mit dem für Sie zuständigen Vertriebsbüro in Verbindung.</p>	
<p>Sollten Sie beabsichtigen, das Produkt in Anwendungen der Luftfahrt, in gesundheits- oder lebensgefährdenden oder lebenserhaltenden Anwendungsbereichen einzusetzen, bitten wir um Mitteilung. Wir weisen darauf hin, dass wir für diese Fälle</p> <ul style="list-style-type: none"> - die gemeinsame Durchführung eines Risiko- und Qualitätsassessments; - den Abschluss von speziellen Qualitätssicherungsvereinbarungen; - die gemeinsame Einführung von Maßnahmen zu einer laufenden Produktbeobachtung dringend empfehlen und gegebenenfalls die Belieferung von der Umsetzung solcher Maßnahmen abhängig machen. 	
<p>Soweit erforderlich, bitten wir Sie, entsprechende Hinweise an Ihre Kunden zu geben.</p>	
<p>Inhaltliche Änderungen dieses Produktdatenblatts bleiben vorbehalten.</p>	
Terms & Conditions of usage	
<p>The data contained in this product data sheet is exclusively intended for technically trained staff. You and your technical departments will have to evaluate the suitability of the product for the intended application and the completeness of the product data with respect to such application.</p>	
<p>This product data sheet is describing the characteristics of this product for which a warranty is granted. Any such warranty is granted exclusively pursuant to the terms and conditions of the supply agreement. There will be no guarantee of any kind for the product and its characteristics. The information in the valid application- and assembly notes of the module must be considered.</p>	
<p>Should you require product information in excess of the data given in this product data sheet or which concerns the specific application of our product, please contact the sales office, which is responsible for you (see www.infineon.com). For those that are specifically interested we may provide application notes.</p>	
<p>Due to technical requirements our product may contain dangerous substances. For information on the types in question please contact the sales office, which is responsible for you.</p>	
<p>Should you intend to use the Product in aviation applications, in health or live endangering or life support applications, please notify. Please note, that for any such applications we urgently recommend</p> <ul style="list-style-type: none"> - to perform joint Risk and Quality Assessments; - the conclusion of Quality Agreements; - to establish joint measures of an ongoing product survey, and that we may make delivery depended on the realization of any such measures. 	
<p>If and to the extent necessary, please forward equivalent notices to your customers.</p>	
<p>Changes of this product data sheet are reserved.</p>	
prepared by: AC	date of publication: 2013-03-06
approved by: MS	revision: 2.3

Appendix B

- IGBT turn-on energy data points extracted from the datasheet for different temperatures:

Table 5 IGBT turn-on energy data points for 25°C

T = 25 °

	0 A	200 A	400 A	600 A	800 A	1000 A	1200 A	1400 A	1600 A	1800 A	2000 A	2200 A	2400 A	2600 A	2800 A
0 V	0 mJ	0 mJ	0 mJ	0 mJ	0 mJ	0 mJ	0 mJ	0 mJ	0 mJ	0 mJ	0 mJ	0 mJ	0 mJ	0 mJ	0 mJ
600 V	0 mJ	9.665 mJ	12.29 mJ	17.54 mJ	23.18 mJ	25.98 mJ	30.09 mJ	29.61 mJ	36.55 mJ	34.73 mJ	35.26 mJ	36.25 mJ	41.05 mJ	40.8 mJ	44.2 mJ

Table 6 IGBT turn-on energy data points for 125°C

T = 125 °

	0 A	200 A	400 A	600 A	800 A	1000 A	1200 A	1400 A	1600 A	1800 A	2000 A	2200 A	2400 A	2600 A	2800 A
0 V	0 mJ	0 mJ	0 mJ	0 mJ	0 mJ	0 mJ	0 mJ	0 mJ	0 mJ	0 mJ	0 mJ	0 mJ	0 mJ	0 mJ	0 mJ
600 V	0 mJ	29.64 mJ	35.36 mJ	47.31 mJ	55.9 mJ	63.1 mJ	70.96 mJ	77.28 mJ	84.23 mJ	90.21 mJ	97.36 mJ	104 mJ	111.8 mJ	118.8 mJ	127.2 mJ

Table 7 IGBT turn-on energy data points for 150°C

T = 150 °

	0 A	200 A	400 A	600 A	800 A	1000 A	1200 A	1400 A	1600 A	1800 A	2000 A	2200 A	2400 A	2600 A	2800 A
0 V	0 mJ	0 mJ	0 mJ	0 mJ	0 mJ	0 mJ	0 mJ	0 mJ	0 mJ	0 mJ	0 mJ	0 mJ	0 mJ	0 mJ	0 mJ
600 V	0 mJ	37.63 mJ	48.19 mJ	59.22 mJ	68.99 mJ	77.95 mJ	87.31 mJ	96.35 mJ	103.3 mJ	112.4 mJ	122.2 mJ	131.1 mJ	140.1 mJ	150 mJ	160.4 mJ

- IGBT turn-off energy data points extracted from the datasheet for different temperatures:

Table 8 IGBT turn-off energy data points for 25°C

T = 25 °

	0 A	200 A	400 A	600 A	800 A	1000 A	1200 A	1400 A	1600 A	1800 A	2000 A	2200 A	2400 A	2600 A	2800 A
0 V	0 mJ	0 mJ	0 mJ	0 mJ	0 mJ	0 mJ	0 mJ	0 mJ	0 mJ	0 mJ	0 mJ	0 mJ	0 mJ	0 mJ	0 mJ
600 V	0 mJ	65.53 mJ	69.08 mJ	113.6 mJ	130.6 mJ	137.5 mJ	168.3 mJ	178.5 mJ	217.6 mJ	239.8 mJ	269.6 mJ	300.8 mJ	333.3 mJ	362.4 mJ	394.4 mJ

Table 9 IGBT turn-off energy data points for 125°C

T = 125 °

	0 A	200 A	400 A	600 A	800 A	1000 A	1200 A	1400 A	1600 A	1800 A	2000 A	2200 A	2400 A	2600 A	2800 A
0 V	0 mJ	0 mJ	0 mJ	0 mJ	0 mJ	0 mJ	0 mJ	0 mJ	0 mJ	0 mJ	0 mJ	0 mJ	0 mJ	0 mJ	0 mJ
600 V	0 mJ	73.36 mJ	99.81 mJ	135.6 mJ	164.3 mJ	191.5 mJ	222.8 mJ	249 mJ	283.3 mJ	313.5 mJ	345.3 mJ	380 mJ	416.3 mJ	452.2 mJ	490.4 mJ

Table 10 IGBT turn-off energy data points for 150°C

T = 150 °

	0 A	200 A	400 A	600 A	800 A	1000 A	1200 A	1400 A	1600 A	1800 A	2000 A	2200 A	2400 A	2600 A	2800 A
0 V	0 mJ	0 mJ	0 mJ	0 mJ	0 mJ	0 mJ	0 mJ	0 mJ	0 mJ	0 mJ	0 mJ	0 mJ	0 mJ	0 mJ	0 mJ
600 V	0 mJ	76.49 mJ	112.1 mJ	144.4 mJ	177.8 mJ	213.1 mJ	244.6 mJ	277.2 mJ	309.6 mJ	343 mJ	375.6 mJ	411.7 mJ	449.5 mJ	488.1 mJ	528.8 mJ

- IGBT conduction loss points extracted from the datasheet:

Table 11 IGBT conduction losses

	0 A	200 A	400 A	600 A	800 A	1000 A	1200 A	1400 A	1600 A	1800 A	2000 A	2200 A	2400 A	2600 A	2800 A
25 °	0.8 V	1 V	1.185 V	1.317 V	1.42 V	1.56 V	1.67 V	1.77 V	1.88 V	1.98 V	2.09 V	2.19 V	2.29 V	2.4 V	2.51 V
125 °	0.8 V	0.97 V	1.185 V	1.41 V	1.58 V	1.76 V	1.92 V	2.09 V	2.25 V	2.41 V	2.58 V	2.74 V	2.92 V	3.08 V	3.24 V
150 °	0.8 V	0.96 V	1.19 V	1.42 V	1.61 V	1.83 V	1.99 V	2.17 V	2.35 V	2.54 V	2.72 V	2.89 V	3.09 V	3.27 V	3.46 V

- Diode conduction loss points extracted from the datasheet:

Table 12 Diode conduction losses point data

	0 A	200 A	400 A	600 A	800 A	1000 A	1200 A	1400 A	1600 A	1800 A	2000 A	2200 A	2400 A	2600 A	2800 A
25 °	0.6 V	1.05 V	1.2 V	1.31 V	1.41 V	1.5 V	1.58 V	1.65 V	1.73 V	1.79 V	1.86 V	1.92 V	2 V	2.05 V	2.09 V
125 °	0.6 V	0.85 V	1.03 V	1.16 V	1.29 V	1.39 V	1.49 V	1.57 V	1.65 V	1.72 V	1.8 V	1.86 V	1.94 V	2.01 V	2.08 V
150 °	0.6 V	0.8 V	0.98 V	1.12 V	1.23 V	1.34 V	1.43 V	1.52 V	1.61 V	1.69 V	1.77 V	1.84 V	1.92 V	1.99 V	2.05 V

- Diode losses during reverse recovery for different temperatures:

Table 13 Losses during reverse recovery for 125°C

T = 125 °

	0 A	200 A	400 A	600 A	800 A	1000 A	1200 A	1400 A	1600 A	1800 A	2000 A	2200 A	2400 A	2600 A	2800 A
-600 V	0 mJ	39.72 mJ	58.82 mJ	78.73 mJ	95.43 mJ	111.1 mJ	125.5 mJ	136.1 mJ	144.2 mJ	150.7 mJ	156.6 mJ	161.6 mJ	166.9 mJ	171.6 mJ	176.7 mJ
0 V	0 mJ	0 mJ	0 mJ	0 mJ	0 mJ	0 mJ	0 mJ	0 mJ	0 mJ	0 mJ	0 mJ	0 mJ	0 mJ	0 mJ	0 mJ

Table 14 Losses during reverse recovery for 150°C

T = 150 °

	0 A	200 A	400 A	600 A	800 A	1000 A	1200 A	1400 A	1600 A	1800 A	2000 A	2200 A	2400 A	2600 A	2800 A
-600 V	0 mJ	47.36 mJ	70.93 mJ	91.5 mJ	113.2 mJ	130.6 mJ	146.1 mJ	157 mJ	165.6 mJ	172.9 mJ	179.9 mJ	186.3 mJ	193.5 mJ	199.4 mJ	207.2 mJ
0 V	0 mJ	0 mJ	0 mJ	0 mJ	0 mJ	0 mJ	0 mJ	0 mJ	0 mJ	0 mJ	0 mJ	0 mJ	0 mJ	0 mJ	0 mJ

- IGBT and diode Foster parameters extracted from the datasheet:

Table 15 Foster parameters of the IGBT chip

	1	2	3	4
R	0.0008 K/W	0.004 K/W	0.0132 K/W	0.0015 K/W
τ	0.0008 s	0.013 s	0.05 s	0.6 s

Table 16 Foster parameters of the diode chip

	1	2	3	4
R	0.002 K/W	0.006 K/W	0.0165 K/W	0.0005 K/W
τ	0.0008 s	0.013 s	0.05 s	0.6 s

- Heatsink and water cooling thermal parameters:

Table 17 Heatsink and water cooling system Foster parameters (SOURCE: Danfysik)

	Thermal resistance [K/W]:	Thermal capacitance [J/K]:
Thermal paste	Rth1=0.0045	Cth1=1
Aluminium heatsink:	Rth2=0.0013	Cth2=300
Water cooling system:	Rth3=0.0057	Cth3=1257

Appendix C

Considering a part of the junction temperature sequence of IGBT1 when the current profile with spike is applied and the water temperature is 21°C, an example of how the Rainflow counting is done is depicted in Figure 50:

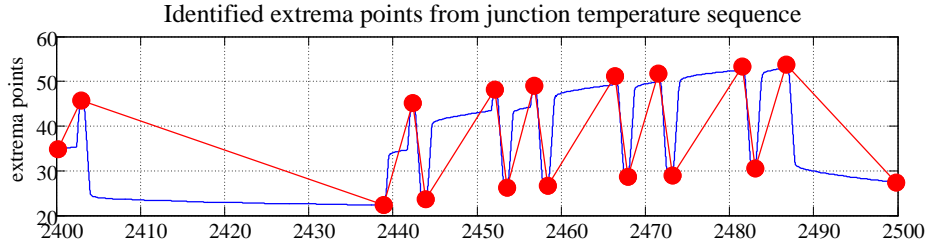


Figure 50 Example of how the extrema are identified on a loading history part

The programme sig2ext.m identifies the first and last point in the time histories also as extreme points besides the other local extrema. In the case of a constant interval, the middle point is taken into account as an extremum (not shown here).

Next, the obtained sequence is counted using Rainflow technique. It has to be kept in mind that the points before the first one at time t=2400s and the ones after t=2600s influence the overall counting and the whole temperature junction counting may look a bit different, but this example is taken out of the big sequence only to show how the counting is performed.

The extrema sequence contains 17 points. The time axis will not be considered anymore, as only the movement on ‘Y-axis’ is important here. However, in the applications where is needed the programmes offers the opportunity to save in the Rainflow matrix also the approximate time of occurrence of the cycle and its ending time.

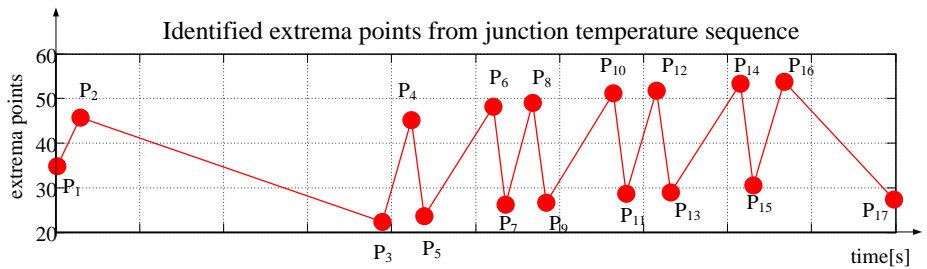


Figure 51 Identified extrema from the loading history

The values of the extrema points is given in Table 18:

Table 18 Values of the identified extrema points

P1	P2	P3	P4	P5	P6	P7	P8	P9	P10	P11	P12	P13	P14	P15	P16	P17
34.8	45.8	22.3	45.2	23.7	48.2	26.2	49	26.7	51.2	28.7	51.8	29	53.4	30.5	53.8	27.4

- P₁ is the first point in the time history. The range $Y = |P_3 - P_2|$ is compared against the range $X = |P_2 - P_1|$. As $Y > X$ and P₁ is the first point in the loading history, a half-cycle is counted from P₁ to P₂ and P₁ is discarded. The range of the half-cycle is calculated using Eq.1:

$$\Delta T_j = |T_{jmax} - T_{jmin}| = |45.8 - 34.8| = 11 \quad \text{Eq. (1)}$$

And average temperature is:

$$T_{jm} = \left| \frac{T_{jmax} + T_{jmin}}{2} \right| = \left| \frac{45.8 + 34.8}{2} \right| = \frac{80.6}{2} = 40.3 \quad \text{Eq. (2)}$$

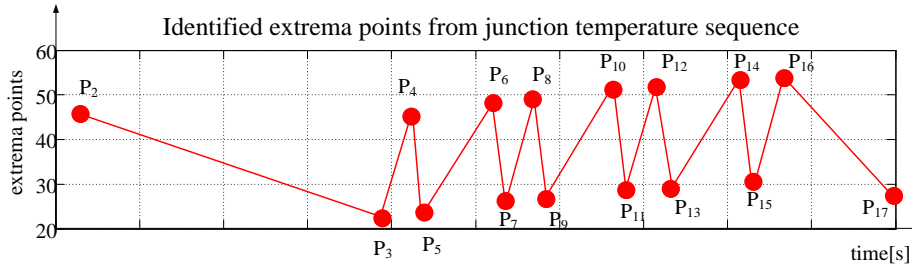


Figure 52 Example of how the three-point check algorithm is working. Removal of P₁

- P₂ represents the new point in the loading history now. The counting is continued with $Y = |P_4 - P_3|$ and $X = |P_3 - P_2|$. As $Y < X$, no cycle is found the algorithm moves forward to a new starting i.e. now point P₃.
- Next, the range $Y = |P_5 - P_4|$ is compared with $X = |P_3 - P_4|$. Again, $Y < X$ and so, no cycle is identified. The algorithm moves forward to point P₄.
- $Y = |P_6 - P_5|$ is compared with $X = |P_5 - P_4|$. $Y > X$, and since P₄ is not the starting point in the history a cycle is identified and both P₄ and P₅ are discarded. P₃ is connected with P₆. The new sequence is depicted in Figure 53:

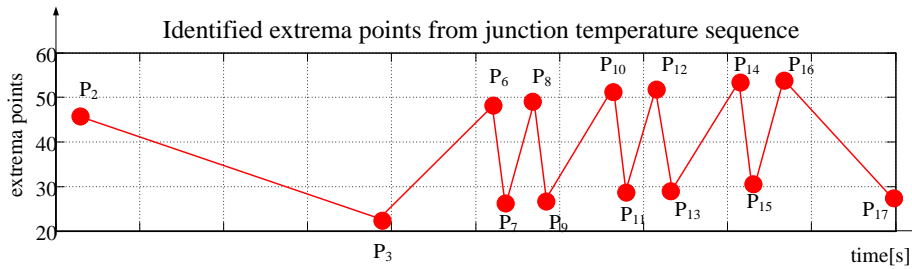


Figure 53 Example of how the three-point check algorithm is working. Removal of P₄ and P₅

- The counting procedure is continued gets restarted from the first point in the loading history – P₂. $Y = |P_6 - P_3|$ is larger than $X = |P_3 - P_2|$. A half cycle is counted from P₂ to P₃ and only point P₂ is discarded.

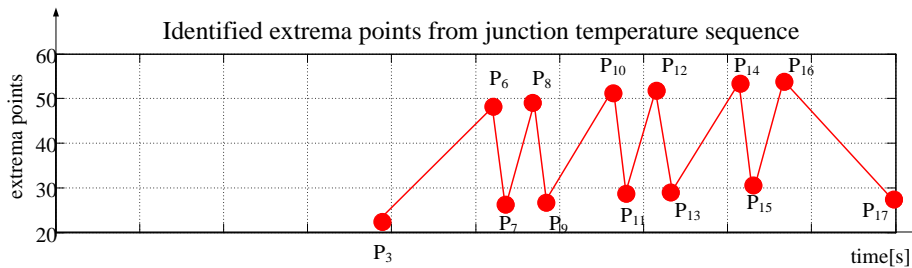


Figure 54 Example of how the three-point check algorithm is working. Removal of P₂

- The counting is started now from P₃. The range $Y = |P_7 - P_6| < X = |P_6 - P_3|$. Therefore no cycle is counted and the algorithm moves forward. The new starting point is P₆. $Y = |P_8 - P_7| > X = |P_7 - P_6|$ and so a cycle is counted from P₆ to P₇ and both points get discarded. P₃ is connected with P₈ now.

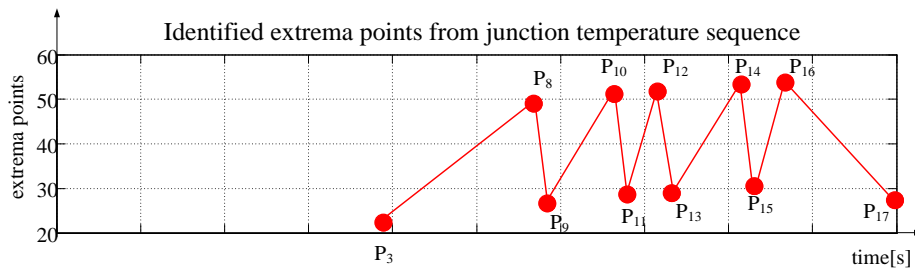


Figure 55 Example of how the three-point check algorithm is working. Removal of P_6 and P_7

- As the range $X = |P_9 - P_8|$ will be larger than the following ranges, the algorithm will always move forward and chose the next starting point. Point P_8 is selected at this step as the starting point. $Y = |P_{10} - P_9| > X = |P_9 - P_8|$ and a cycle is counted from P_8 to P_9 . Both points are discarded and P_3 is connected with P_{10} .

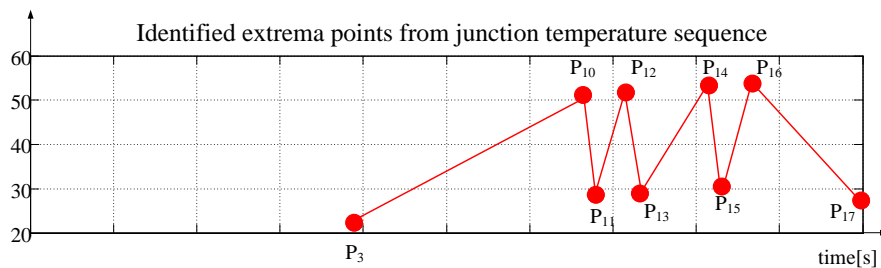


Figure 56 Example of how the three-point check algorithm is working. Removal of P_8 and P_9

- Range $Y = |P_{11} - P_{10}| < X = |P_{10} - P_3|$, so the new starting point is chosen as P_{10} . $Y = |P_{12} - P_{11}| > X = |P_{11} - P_{10}|$ and a cycle is counted from P_{10} to P_{11} . Both points are discarded and P_3 is connected with P_{12} .

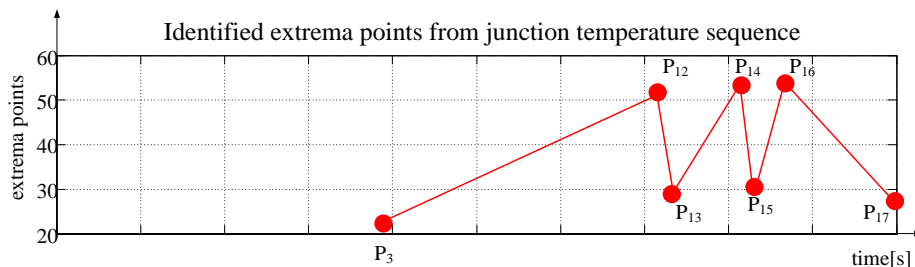


Figure 57 Example of how the three-point check algorithm is working. Removal of P_{10} and P_{11}

- Range $Y = |P_{13} - P_{12}| < X = |P_{12} - P_3| \rightarrow$ new starting point: P_{12} . $Y = |P_{14} - P_{13}| > X = |P_{13} - P_{12}|$ and a cycle is counted from P_{12} to P_{13} . Both points are discarded and P_3 is connected with P_{14} .

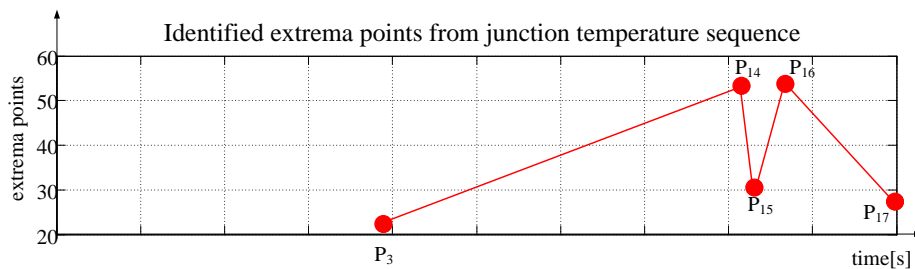


Figure 58 Example of how the three-point check algorithm is working. Removal of P_{12} and P_{13}

- Range $Y = |P_{15} - P_{14}| < X = |P_{14} - P_3| \rightarrow$ new starting point: P_{14} . $Y = |P_{16} - P_{15}| > X = |P_{15} - P_{14}|$ and a cycle is counted from P_{14} to P_{15} . Both points are discarded and P_3 is connected with P_{16} .

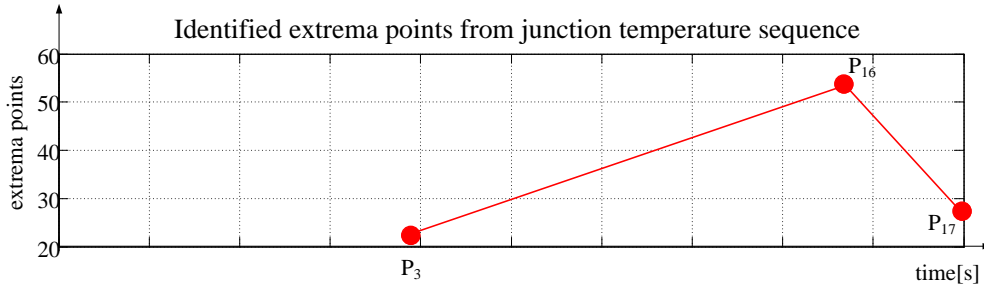


Figure 59 Example of how the three-point check algorithm is working. Removal of P14 and P15

- Range $Y = |P_{17} - P_{16}| < X = |P_{16} - P_3| \rightarrow$ new starting point: P_{16} . The algorithm should continue with point P_{16} , but since there are only 2 points left it start from the beginning over again. No cycle can be found and the two remaining ranges are counted as half cycle: one from P_3 to P_{16} and another one from P_{16} to P_{17} . The algorithm ends here.

All the mean temperatures and temperature differences are calculated according to Eq. 1 and Eq. 2. The results of the counting in the order of occurrence of the cycles and half cycle are summarized in the table below:

Table 19 Rainflow matrix containing the temperature ranges, mean temperature and number of cycles

ΔT	11	21.5	23.5	22	22.3	22.5	22.8	22.9	31.5	26.4
T_m	40.3	34.45	34.05	37.2	37.85	39.95	40.4	41.95	38.05	40.6
n	0.5	1	0.5	1	1	1	1	1	0.5	0.5

The whole counting can be visualized by running rfdemo1.m:

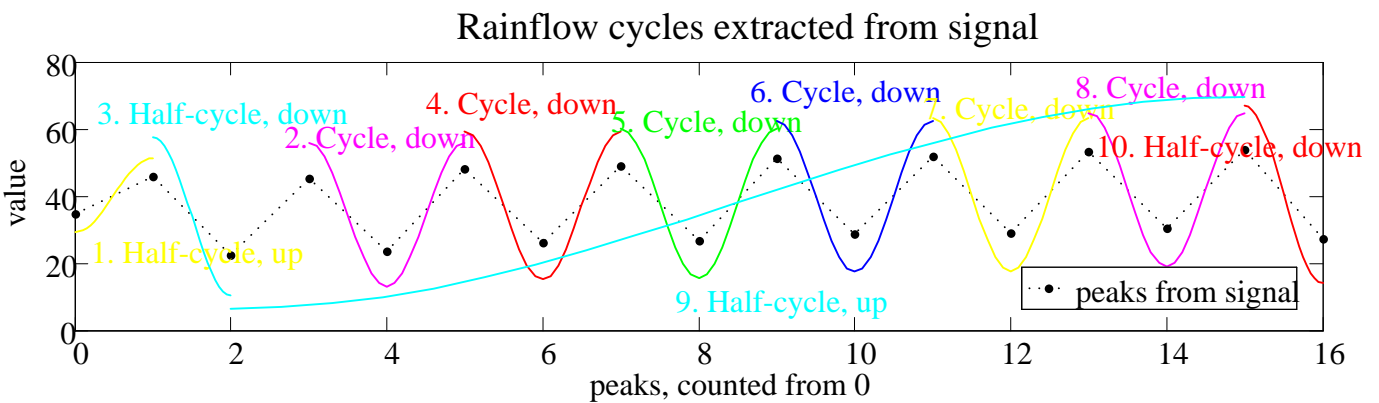


Figure 60 Example of how the Rainflow three point check algorithm is done using Matlab

The distribution of difference in temperature and mean temperature among cycles and half cycles is visualized in a 3D matrix by running rfmatrix.m:

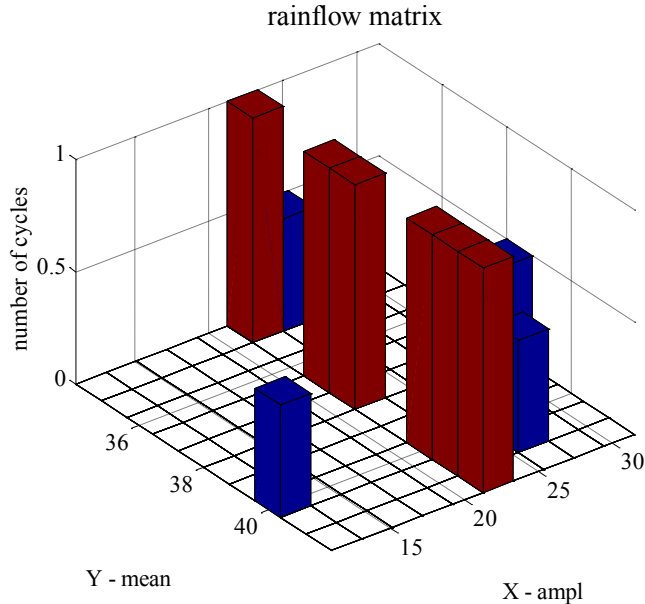


Figure 61 Rainflow 3D matrix containing the range (shown here as twice the amplitude), mean stress and number of cycles

The distribution of mean temperature or temperature range among the counted cycles can be visualized also with histograms as the ones in Figure:

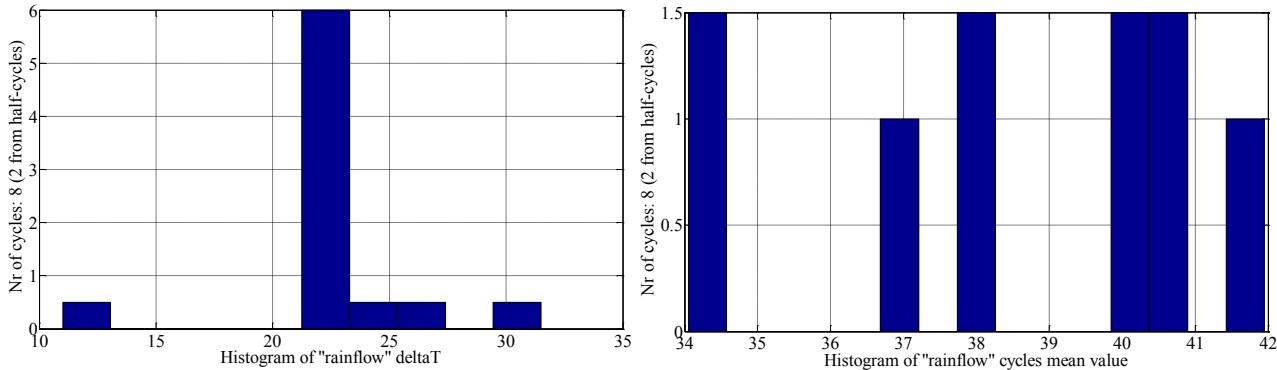


Figure 62 Rainflow histogram of the distribution of range temperature among the identified cycles (left) and the damage cause by the ranges (right)